RESEARCH ARTICLE

Polymer-Based 3-D Printed 140 to 220 GHz Metal Waveguide Thru Lines, Twist and Filters

ROSHAN PAYAPULLI[1], LIYAN ZHU[1], SANG-HEE SHIN[1,2], (Member, IEEE),
MANOJ STANLEY[2], (Member, IEEE), NICK M. RIDLER[2], (Fellow, IEEE),
AND STEPAN LUCYSZYN[1], (Fellow, IEEE)

[1]Department of Electrical and Electronic Engineering, Imperial College London, SW7 2AZ London, U.K.
[2]National Physical Laboratory, Department of Electromagnetic and Electrochemical Technologies, TW11 0LW Teddington, U.K.

Corresponding author: Stepan Lucyszyn (s.lucyszyn@imperial.ac.uk)

ABSTRACT This paper demonstrates the current state-of-the-art in low-cost, low loss ruggedized polymer-based 3-D printed G-band (140 to 220 GHz) metal-pipe rectangular waveguide (MPRWG) components. From a unique and exhaustive up-to-date literature review, the main limitations for G-band split-block MPRWGs are identified as electromagnetic (EM) radiation leakage, assembly part alignment and manufacturing accuracy. To mitigate against leakage and misalignment, we investigate a 'trough-and-lid' split-block solution. This approach is successfully employed in proof-of-concept thru lines, and in the first polymer-based 3-D printed 90° twist and symmetrical diaphragm inductive iris-coupled bandpass filters (BPFs) operating above 110 GHz. An inexpensive desktop masked stereolithography apparatus 3-D printer and a commercial copper electroplating service are used. Surface roughness losses are calculated and applied to EM (re-)simulations, using two modifications of the Hemispherical model. The 7.4 mm thru line exhibits a measured average dissipative attenuation of only 12.7 dB/m, with rectangular-to-trapezoidal cross-sectional distortion being the main contributor to loss. The 90° twist exhibits commensurate measured performance to its commercial counterpart, despite the much lower manufacturing costs. A detailed time-domain reflectometry analysis of flange quality for the thru lines and 90° twists has also been included. Finally, a new systematic iris corner rounding compensation technique, to correct passband frequency down-shifting is applied to two BPFs. Here, the 175 GHz exemplar exhibits only 0.5% center frequency up-shifting. The trough-and-lid assembly is now a viable solution for new upper-mm-wave MPRWG components. With this technology becoming less expensive and more accurate, higher frequencies and/or more demanding specifications can be implemented.

INDEX TERMS Additive manufacturing, 3-D printing, millimeter-wave, G-band, WR-5, rectangular waveguide, 90° twist, TDR, butterworth filter, surface roughness.

I. INTRODUCTION

3-D printing, one form of additive manufacturing, is rapidly gaining popularity for rapid prototyping and small-batch manufacturing of bespoke passive microwave, millimeter (mm)-wave and terahertz (THz) components. When compared with formative and subtractive manufacturing (collectively referred to here as machining technologies), in general,

The associate editor coordinating the review of this manuscript and approving it for publication was Debashis De[ID].

it offers the potential for weight reduction, minimal waste, the ability to manufacture more geometrically complex structures, fast turnaround and significant cost savings.

Polymer-based 3-D printing enables further mass reduction and cost savings when compared with metal-based 3-D printing, but fabricated parts have poorer structural rigidity and non-conductive surfaces. Therefore, ruggedization in the design phase and metalization in the manufacturing phase are necessary. Nevertheless, polymer-based 3-D printing has greater potential for aerospace applications, where mass

reduction is critical. To this end, Imperial College London (ICL) recently demonstrated a fully polymer-based 3-D printed G-band (140 to 220 GHz) integrated front-end subsystem [1], based on the design of a passive microwave radiometer. This work combines quasi-optical [2] and metal-pipe rectangular waveguide (MPRWG) components [3].

When compared to transmission lines (e.g., microstrip or coplanar waveguide), MPRWGs exhibit much lower dissipative attenuation (due to ohmic losses), having infinite isolation and a much higher power handling capacity, making them essential for applications that require high sensitivity (e.g., radiometry, communications and radar) or high output power (e.g., communications and radar). Commercially machined waveguides are typically manufactured either by drawing through a rectangular die (formative), computerized numerically controlled (CNC) milling (subtractive) or electronic discharge machining (EDM) with spark erosion (subtractive). As a result, commercially made MPRWGs are typically slow and expensive to fabricate, and are significantly heavier than transmission lines. Manufacturing costs are exacerbated at upper-millimeter-wave frequencies (*ca.* 100 GHz to 300 GHz), as smaller apertures and internal features require greater mechanical accuracy.

Polymer-based 3-D printing represents a promising alternative. For example, the authors have previously reported a number of MPRWG components operating up to 1.1 THz [4], [5], [6], [7], [8]. In general, above D-band (110 to 170 GHz), high-cost printing has been required, often with custom-developed metal plating techniques, which substantially reduces cost savings. Furthermore, little has been reported on polymer-based 3-D printing of MPRWG components with added functionality (e.g., twisting or filtering) above W-band (75 to 110 GHz). This paper investigates the design, fabrication and measurement of low-cost G-band MPRWG components.

In Section II, a unique and exhaustive up-to-date literature review is undertaken for 3-D printed thru lines above 75 GHz, 90° twists above 8 GHz and BPFs above 75 GHz. To the best of our knowledge, all metal- and polymer-based exemplars have been included, giving valuable insight into the main design challenges for each component type.

In Section III, a new MPRWG design that can be manufactured using an ultra-low-cost desktop masked stereolithography apparatus (MSLA) printer and a commercial copper electroplating service is presented. This manufacturing process, which is normally associated with applications below 110 GHz, is extended to 220 GHz by introducing a 'trough-and-lid' assembly. Here, a split-block design is employed, where waveguides are manufactured in two separate parts and later assembled, using an unorthodox H-plane *a*-edge split and lips that extend beyond the sidewalls to connect with the upper wall. A good electrical/electromagnetic (EM) seal is formed between the bottom and top parts of the MPRWG, to mitigate against gap formation and, thus, electromagnetic radiation leakage. This solution was used here to manufacture thru lines, 90°

twists and symmetrical diaphragm inductive iris-coupled Butterworth BPFs, all exhibiting relatively low loss (i.e., comparable dissipative attenuation to commercial-off-the-shelf (COTS) components).

Successful BPF design also requires consideration of the manufacturing accuracy limitations associated with MSLA printing. For correcting the passband down-shifting effects of iris corner rounding (ICR), a unique systematic compensation technique is applied to the designs of two 5th order Butterworth BPFs, with design center frequencies of 155 GHz and 175 GHz. We previously applied this technique to transverse-offset inductive iris BPFs, but without any introduction or discussion [1]. This new compensation technique is different to the quantization predistortion that we recently applied to BPFs at G-band [9]. Our low-loss trough-and-lid assembly solution, discussed here, was also employed in our previous D-band [10] and G-band MPRWG demonstrators [1], [9], but again without any introduction or discussion.

In Section IV, the fabrication procedure is given, including analysis of the 3-D printed component cost savings. Our outsourcing plating costs are high, when compared to the 3-D printing, but the overall cost is still low. In Section V, conductor surface roughness is investigated to account for excess insertion loss. Finally, measurement results are discussed in Section VI. This includes a detailed time-domain reflectometry (TDR) analysis for the thru lines and 90° twists.

In summary, this paper presents a unique literature review of (sub-)THz 3-D printed thru lines, twists and BPFs. Our 3-D printed trough-and-lid assembly is introduced and discussed in detail. This paper also demonstrates the first polymer-based 3-D printed MPRWG 90° twists and symmetrical diaphragm inductive iris-coupled BPFs operating above 110 GHz, highlighting the potential for the trough-and-lid assembly with upper-mm-wave MPRWGs. Also, for the first time, a systematic ICR compensation technique is introduced. A detailed TDR analysis is included in the characterization of the thru lines and twists; the first instance of its application with 3-D printed MPRWGs.

II. LITERATURE REVIEW
A. THRU LINES
Thru lines are defined here as straight sections of waveguide, used as interconnects between two other components. They are the simplest MPRWG structure, representing a useful benchmark for assessing performance. Upper- and sub-millimeter-wave (300 GHz to 3 THz) COTS waveguides are generally precision-machined with two split-block parts that are joined using brazing techniques.

From an exhaustive search, 16 examples of 3-D printed thru lines operating above 75 GHz were found in the open literature; all references published since 2015. A summary is given in Table 1, where α'_D and *RL* refer to the respective average dissipative attenuation per unit length and worst-case return loss across its waveguide band.

The former enables a direct comparison between thru lines with the same waveguide band, and is discussed further in Section VI. In addition, nine COTS thru lines are included, for comparison.

The submillimeter seamless (single-block) waveguide product range from Flann Microwave Ltd. includes low loss COTS thru line components operating up to 1.1 THz [11]. The nominal insertion loss, measured at the lower band-edge frequency f_L, is shown in Table 1. Either copper or nickel is electroformed (formative) to create the MPRWG, having a quoted internal mean profile surface roughness of $R_a < 0.2$ μm. The performance is commensurate with commercially machined waveguides having a split-block construction [11]. Further analysis is given in Section V.

Single-block metal-based 3-D printed thru lines have been demonstrated at D-band and J-band (220 to 325 GHz) by Zhang and Zirath, using selective laser melting (SLM) [12]. No additional plating was required, as the SLM printer uses a copper alloy powder. The reported measured α'_D values are 19 dB/m and 121 dB/m for 50 mm long thru lines at D- and J-bands, respectively; these are 10 dB/m and 88 dB/m for their respective COTS counterparts [12].

The difference in α'_D, between those from metal-based 3-D printed and COTS thru lines, can be attributed to ohmic losses, principally due to poor intrinsic bulk DC conductivity of the metal alloy powders, and high surface roughness. Also, due to the high costs associated with metal-based 3-D printers, fabrication may employ outsourcing services.

Polymer-based 3-D printing has been shown to produce low loss (sub-)THz thru lines, as demonstrated by von Bieren et al. at J-band, using a single-block design [18]. Fabrication was undertaken using a high-resolution stereolithographic apparatus (SLA) printer, providing dimensional accuracy to within only ± 10 μm, followed by their custom-developed copper plating process. The measured α'_D is only 13 dB/m; an order of magnitude improvement (in dB/m) over the previous metal-based exemplar [12].

The authors previously demonstrated polymer-based 3-D printed thru lines above G-band, using two different high-cost manufacturing techniques. First, single-block 500 to 750 GHz (WM-380) and 750 GHz to 1.1 THz (WM-250) exemplars were fabricated using the University of Tokyo's experimental ultra-high-resolution RECILS 3-D printer [20] and a commercial electroless plating process [8]. With the former the mid-band α'_D is 240 dB/m, which is significantly poorer than the COTS counterpart, having 65 dB/m. Second, a 325 to 500 GHz split-block thru line was fabricated by outsourcing high-resolution polymer-jet (Polyjet) 3-D printing, with 500 nm thick copper sputter coating; the average α'_D is 440 dB/m. Radiation leakage from the split is believed to be the major loss mechanism. This is caused by a break in the transverse current path, due to a physical gap between assembled parts. Neither of these exemplars can be considered low loss MPRWG components.

An example of low-cost manufacturing (i.e., with total manufacturing costs being low in comparison to the retail costs of typical COTS counterparts) uses a desktop polymer-based SLA printer and a simple silver-copper electroless plating process [16], [21]. This was used to produce a D-band single-block 25.4 mm long thru line [15], with an average measured α'_D of 26 dB/m (comparable to a COTS thru line).

Until now, at G-band, the authors reported the only previous example of a low-cost 3-D printed thru line, employing a traditional symmetrical E-plane split-block design and a desktop SLA printer [3]. This first attempt demonstrated a high α'_D of 59 dB/m, due to radiation leakage from the split. It will be shown in this paper that low loss can be achieved with our unconventional H-plane split-block design and a low-cost MSLA printer.

B. 90° TWISTS
A MPRWG connection between orthogonally polarized waveguide ports can be provided by a physical rotation of 90°. At upper-millimeter-wave frequencies, commercial twists are normally realized by forced mechanical rotation of a straight MPRWG thru line about its longitudinal axis [22], resulting in a smooth transition. This may cause internal physical defects and poor structural rigidity; the end result being even more expensive than the original thru line.

Alternatively, 90° twists can also be manufactured through precision-machining, by using novel designs. Examples include a stepped rotation twist at W-band [23], shaped channel transition at J-band [24] and a rectangular-square-rectangular transition at WM-380 [25]. However, their multiple wave impedance discontinuities, which are inherent with these full waveguide band transitions, will result in a degraded return loss performance and, therefore, higher insertion loss when compared with smooth transitions.

Smooth transitions can be easily manufactured using formative and low-cost additive manufacturing. From an exhaustive literature review, 15 examples of 3-D printed 90° twists were found, operating above 8 GHz. A summary is given in Table 2; all references published since 2016. In addition, three COTS 90° twists are included, for comparison.

Here, IL refers to the average insertion loss for the discrete twist across the waveguide band. 'Rotational Smoothness' refers to the degree of rotation per λ_{gL} for smooth twists, where λ_{gL} is the guided wavelength at the lower band-edge frequency (having the worst-case attenuation), or step length per λ_{gL} for stepped twists. As can be seen for the WR-10 COTS twists, in Table 2, a lower value of rotational smoothness gives a better return loss, but at the expense of a degraded insertion loss.

The majority of the examples are integrated with one or more functionalities, as a single component or within a multi-component subsystem. This demonstrates the capability of 3-D printing for manufacturing complex waveguide geometries; avoiding the need for inter-stage flange-to-flange

TABLE 1. Millimeter-wave 3-D printed and COTS thru lines. (*Nominal worst-case insertion loss found at the lower band-edge frequency f_L and † COTS components measured by the authors).

Frequency Range (GHz) [Waveguide Band]	α'_D (dB/m)	RL (dB)	Length (mm)	Split-Block	Manufacturing Technologies		Year	Ref.
					Printed/COTS	Plating		
65-90 [WR-12]	7.5	10	50	No	SLM (Cu-15Sn)	None	2016	[12]
75-110 [WR-10]	4.3†	25†	50	No	COTS (Al)	Au	2022	[13]
	5.5	25	100		SLA	Proprietary Cu plating	2017	[14]
	6.3	17	25.4			Ag and Cu electroless	2017	[15]
	8.3	18	100		MLS (AlSi10Mg)	None	2017	[14]
	11	20	60	E-plane symmetrical	SLA	30 µm Cu electroplating	2015	[4]
	14.0	21	25.4		DLP	Ag electroless	2016	[16]
110-170 [WR-6]	11.5*	-	100	No	COTS	Au	2023	[11]
	19	20	50		SLM (Cu-15Sn)	None	2016	[12]
	25.6	-	25.4		SLA	Ag and Cu electroless	2017	[15]
140-220 [WR-5]	9.4†	27†	50.8	No	COTS (Al)	Au	2022	[17]
	9.9†	28†	25.4					
	12.7	15	7.4	H-plane a-edge	MSLA	50 µm Cu electroplating	2022	**This work**
	13.7	14	10.4					
	17*	-	100	No	COTS	Au	2023	[11]
	59	6	50.8	E-plane symmetrical	SLA	20 µm Cu electroplating	2018	[3]
220-325 [WR-3]	13	-	25		SLA	Custom-developed Cu plating	2014	[18]
	31*	-	100		COTS	Au	2023	[11]
	120	12	50	No	SLM (Cu-15Sn)	None	2016	[12]
325-500 [WM-570]	36	-	25.4		RECILS	3.6 µm Ni, Cu and Au electroless	2022	[19]
	61*	-	100		COTS	Au	2023	[11]
	440	-	25	H-plane a-edge	Polyjet	500 nm Cu sputter coating	2017	[7]
500-750 [WM-380]	115*	-	100		COTS	Au	2023	[11]
	240	7	5	No	RECILS	1 µm Ag electroplating	2017	[8]
750-1100 [WM-250]	230*	-	100		COTS	Au	2023	[11]
	1,400	6	5		RECILS	1 µm Ag electroplating	2017	[8]

coupling and, therefore, reducing wave impedance mismatch losses. With all integrated twists, *IL* and *RL* measurements were not available for the discrete component.

Zhang et al. demonstrated the integration of two functionalities into a single component at Ka-band (26.5 to 40 GHz): a 90° twist and a 4th order Chebyshev diaphragm inductive iris-coupled BPF [34]. Fabrication involves SLA printing and copper electroplating. Measured results show 0.81 dB average passband insertion loss and 0.36% frequency down-shifting from the designed BPF center frequency. Peverini et al. demonstrated the integration of three functionalities into a single component at Ku-band; a 90° twist, a low-pass filter and a 90° bend [28]. Measured results exhibit 0.12 dB average passband insertion loss and greater than 60 dB stopband rejection.

With multi-component subsystems, Dimitriadis et al. demonstrated a fixed Ka-band single-block 2 × 2 conical horn antenna array, with a waveguide feeding network consisting of three 3 dB power splitters, two smooth transition 90° twists, two smooth 90° bends and four 90° miter bends [32], using an SLA printer and electroless copper plating. Measured results show an antenna gain of 19-23 dBi across Ka-band.

More recently, the authors demonstrated the first fully 3-D printed tunable microwave subsystem, consisting of 26 circuit elements, creating a Ku-band steerable 4-element phased array antenna [5]. The main MPRWGs were fabricated using Polyjet and copper electroplating. The subsystem integrated three 3 dB power splitters, four dielectric-insert tunable phase shifters, four smooth transition 90° twists and four H-plane

TABLE 2. Microwave and millimeter-wave 3-D printed 90° twists operating above 8 GHz. (*measured step length/λ_{gL} and †COTS components were measured by the authors).

Frequency Range (GHz) [Waveguide Band]	IL (dB)	RL (dB)	Total Length (mm)	Twist Type	Rotational Smoothness (°/λ_{gL})	Integration	Split-Block	Manufacturing Technologies Printed/COTS	Plating	Year	Ref.
8-12 [WR-90]	-	-	109	Smooth	54	BPF	No	SLA	Cu electroplating	2021	[26]
12-18 [WR-62]	-	-	-		-	Power splitter, 90° bends, BPFs, horn antenna array			20 μm Cu and Sn electroplating	2019	[27]
	-	-	-		-	Power splitters, 90° bends, phase shifters, horn antenna array	H-plane symmetrical	Polyjet	20 μm Cu electroplating	2019	[5]
15-22 [WR-51]	-	-	63	Smooth	58	90° bend, BPF		SLA	Cu	2022	[28]
	-	-	47, 63, 79		60, 45, 36	90° bend, BPF		SLM (AlSi10Mg)	None	2018	[29]
26.5-40 [WR-28]	-	-	-		-	Orthogonal Mode Transducer (OMT)		MLS (AlSi10Mg)		2019	[30]
	-	-	-		-	90° bend, OMT, slotted antenna			5 μm Cu electroless	2017	[31]
	-	-	-		-	Power splitters, 90° bends, horn antenna array	No	SLA	Cu electroless	2017	[32]
	-	-	20.6	Stepped	0.28*	BPF			11 μm Cu and Ag electroplating	2020	[33]
	-	-	44.3		38	BPF			11 μm Cu and Ag electroplating	2019	[34]
	-	-	-	Smooth	-	Power splitters, turnstile junction, OMT		MLS (AlSi10Mg)	None	2022	[35]
	-	-	-		-	Diplexer, OMT		DLP	Ag electroless	2020	[36]
75-110 [WR-10]	0.10†	25†	31.75	Smooth	31	None		COTS (Al)	Ag	-	[37]
	0.21	26.4	42		20	None		COTS (Al)	Au	2022	[38]
	0.21	22	4.7	Stepped	0.18*	None		MLS (Stainless steel)	None	2016	[23]
140-220 [WR-5]	0.62	13.2	31.75	Smooth	18	None	H-plane *a*-edge	MSLA	50 μm Cu electroplating	2022	**This work**
	0.62†	12.9†	31.75		18	None	No	COTS (Cu)	Au	-	[39]

sectoral horn antennas. The total measured beam steering angle is approximately ±27° at 15 GHz and 17 GHz.

In summary, polymer-based 3-D printed 90° twists have already been demonstrated up to 110 GHz. It will be shown here that a G-band 90° twist can be realized by modifying the design of a low loss thru line.

C. BANDPASS FILTERS

BPFs with lower insertion loss and narrower fractional bandwidths require suitably high quality (Q-)factor resonators, which can be implemented using MPRWGs.

At microwave (0.3 to 30 GHz) and lower-millimeter-wave frequencies (30 to *ca.* 100 GHz), the associated linear dimensions (i.e., lengths and widths of both the cavities and their coupling irises) are significantly larger than the minimum feature size of most manufacturing technologies, even with low-cost printers. However, for a constant bandwidth, higher operational frequency BPFs require higher loaded Q-factors (Q_L) and smaller dimensions. Therefore, the range of suitable printer technologies is further limited. Poor manufacturing accuracy can result in significant frequency shifting, primarily due to errors in cavity dimensions. Moreover, significant changes in the

bandwidth can be found, primarily due to errors in iris dimensions. In extreme cases, the desired filter response can be distorted beyond acceptable limits.

As a result, almost all sub-THz (*ca.* 100 to 300 GHz) MPRWG BPFs reported in the open literature employ high-accuracy micromachining technologies, achieving close agreement with design specifications. Examples include CNC milling [40] and laser micromachining [41] at W-band, SU8 micromachining at J-band [42] and deep reactive-ion etching (DRIE) at WM-250 [43]. A full literature review of micromachined sub-THz COTS MPRWG BPFs has already been published [9].

From an exhaustive literature review, 12 examples of 3-D printed BPFs operating above 75 GHz were found. A summary is given in Table 3; all references published since 2015. Here, f_0, BW, and FBW refer to the center frequency, 3 dB bandwidth and fractional bandwidth, respectively. Note that $FBW = BW/f_0$ is based on designed values, while 'Measured Q_L' is based on the measured 3 dB fractional bandwidth. With the exception of our chained-function BPF [9], all other filters were Chebyshev. In all cases, TE_{101} mode rectangular cavity resonators were employed, with the majority using symmetrical diaphragm

inductive irises. Two exceptions use either transverse offset inductive irises [9] or asymmetrical diaphragm capacitive irises [44].

Metal-based printing has also been adopted, with different types of cavity resonator that include: shaped rectangular and slotted spherical at X-band [45], [46], depressed super-ellipsoid at Ku-band [47] and rectangular cavity at W-band [48], G-band [49] and J-band [44]. As expected, higher insertion loss is measured, when compared to machined BPFs, due to lower effective bulk DC conductivity and larger surface roughness.

Polymer-based printed BPFs have also been widely demonstrated, with slotted dual-mode circular waveguide resonators at X-band [50], gap waveguides at Ka-band [51] and rectangular cavity resonators at W-band [4]. As expected, passband insertion loss is lower than exemplars that use metal-based printing. However, in general, greater center frequency shifting occurs due to lower accuracy. Furthermore, several types of manufacturing accuracy limitations with polymer-based printing do not exist in metal-based technologies.

These include: (i) pixel quantization errors, associated with MSLA printing [9]; (ii) significant iris corner rounding (ICR), due to either material erosion or resin residues; (iii) warping, due to uneven cooling-based contraction; and (iv) shrinkage during UV post-curing.

For BPFs, manufacturing accuracy limitations can be divided into two categories: dimensional and geometrical. The former refers to discrepancies between the designed and manufactured linear dimensions. The latter refers to changes in resonator and iris geometries. The authors have previously developed a pre-distortion technique for pixel quantization errors, associated with MSLA printing, being one type of dimensional inaccuracy [9]. With the latter, addressed in this paper, ICR is the main type of geometrical inaccuracy found with low-cost polymer-based printers. Here, the resulting passband frequency shifting is investigated. It will be shown that good results can be achieved using our new ICR compensation technique, when applied to G-band BPFs.

III. G-BAND DESIGNS

A. THRU LINES

Standard WM-1295 [54] MPRWGs have internal cross-sectional dimensions of only 1,295 μm $\times$ 647.5 μm for G-band operation (equivalent to WR-5), with the flange design based on IEEE standard specifications [55]. All 3-D computer-aided design (CAD) drawings are undertaken using Autodesk Fusion 360.

With single-block designs, the small aperture dimensions for WR-5 MPRWGs makes conventional electro- or electroless plating impractical. In contrast, a split-block design can provide plating fluids with improved internal access to the waveguide, ensuring sufficient metalization with conventional copper electroplating. In theory, a conventional symmetrical E-plane split will have less loss attributed to

radiation leakage with high quality manufactured waveguides, as no transverse currents flow across the center of the broad wall with TE_{10} mode propagation. However, with polymer-based printing at G-band, any gap is likely to cause significant radiation leakage. Furthermore, any misalignment between assembled split-block parts will cause significant cross-sectional distortion, which degrades the return loss.

Against conventional wisdom, our MPRWGs are constructed by printing the waveguide and all internal features on the bottom part, with the split made along the broad sidewall, as a solution to avoid assembly misalignment. This is referred to here as an H-plane a-edge split; the nomenclature is derived from Stil et al. [56], where an E-plane split along the narrow sidewall is defined as a b-edge. Further advantages for this construction include the easier removal of resin residue, easier integration of external components and the ability to inspect and measure complete waveguide features (discussed in Section III.C.). Note that H-plane a-edge splits have already been reported in 3-D printed MPRWGs at S-band [57], X-band [58], Ka-band [59], D-band [10], G-band [1] and WM-570 band [7], with four of these examples integrating external components.

To mitigate against radiation leakage, candidate techniques from subtractive manufacturing include brazing, RF chokes [60], pin wall joints [61] and photonic crystal joints [62]. These are unsuitable here, due to the polymer's inability to withstand high temperatures, its inherent softness, and post-production warping. Instead, our design employs 'lips' that form part of the sidewalls, to connect with the upper wall, to provide a good electrical/EM seal with tight assembly. This is illustrated in Fig. 1, with a and b referring to the internal aperture width and height, respectively. The lip width W and lip height H are set to 550 μm and 200 μm, respectively. The full split-block structure is referred to here as the 'trough-and-lid' assembly.
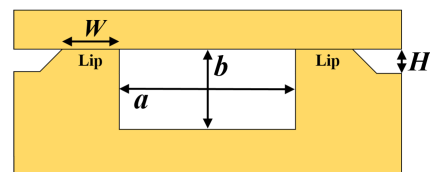

FIGURE 1. Flange view illustration of the trough-and-lid assembly, showing lips in contact with the flat top part.

While having been developed independently for 3-D printing by the authors, a recent online search found a similar approach with commercially-available machined mixers at W-band [63] and G-band [64]. Since machined parts are very rigid, any significant inaccuracy may result in small gaps to appear between the lips and the lid, resulting in radiation leakage. In contrast, with polymer-based printing, there is some degree of malleability that helps to close small gaps.

Finally, to advance the technology readiness level of polymer-based printing for aerospace applications, all MPRWG components are ruggedized, to improve structural

TABLE 3. Millimeter-wave 3-D printed MPRWG BPFs. (*our previously reported transverse offset iris †Chebyshev and ‡chained-function BPFs [9]).

| f_0 (GHz)	FBW (%)	Waveguide Band [Filter Order]	IL (dB)	RL (dB)	Measured Q_L	Split-Block	Technology Printer	Technology Plating	f_0 Shift (%)	BW Shift (%)	Coupling	Year	Ref.
73.5	6.8	WR-12 [15]	8.0	8	18.9	No	MLS (CuSn15)	None	+2.7	-20	Symmetrical Diaphragm Inductive Iris	2015	[52]
83.5	6.0	WR-12 [11]	3.0	9	14.5				+4.2	+20			
90	11.1	WR-10 [5]	0.4	18	6.7		SLA	10 μm Cu electroplating	-2.8	+10		2016	[41]
90	11.1		1.0	15	7.3		MLS (Stainless steel)	5 μm Cu electroplating	-1.0	-0.1		2019	[48]
			1.9	18	7.0			None	-1.8	+0.7			
91.3	7.8	WR-10 [4]	1.4	7.6	12.2	E-plane symmetrical	SLS (Polyamide)	Cu electroplating	-3.8	+1.4		2020	[53]
100	10	WR-10 [6]	1.0	11	15.8		SLA	30 μm Cu electroplating	+7.2	-32		2015	[4]
155	10	WR-05 [5]	0.47	10	11.2	H-plane a-edge	MSLA	50 μm Cu electroplating	+2.3	-8.4	Symmetrical Diaphragm Inductive Iris	2022	**This work**
175			0.44	13	11.5				+0.5	+13			
180	11	WR-5 [5]	2.9	18	7.2	No	MLS (Stainless steel)	None	-1.4	+21	Symmetrical Diaphragm Inductive Iris	2020	[49]
			3.0	18	7.1				-1.5	+21			
183	9.3		0.55†	6†	7.7†	H-plane a-edge	MSLA	50 μm Cu electroplating	-3.3†	+11†	Transverse Offset Inductive Iris	2022	[9]*
			0.55‡	13‡	5.8‡				-0.9‡	+15‡			
300	10.5	WR-3 [5]	1.1	10	8.0	E-plane symmetrical	MLS (Stainless steel)	3 μm Au electroless	-1.2	+6.8	Asymmetrical Diaphragm Capacitive Iris	2021	[44]
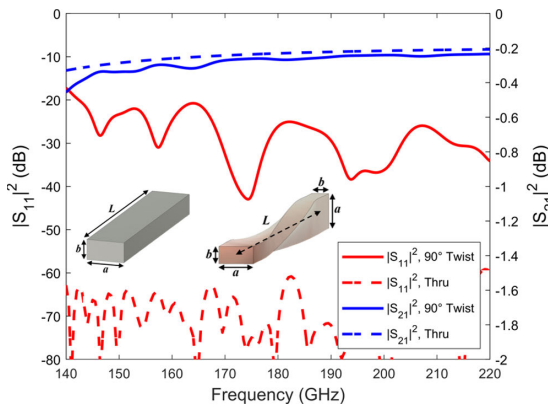
FIGURE 2. HFSS simulation results for the WR-5 thru and 90° twist (insets show internal CAD layouts of the components) having length $L = 31.75$ mm.

rigidity. Two lengths of 3-D printed thru line are manufactured and tested: 7.4 mm and 10.4 mm.

B. 90° TWISTS

Two G-band COTS 90° twists, manufactured by Pasternack Enterprises Inc., have a flange-to-flange component length of 1.25 inches (31.75 mm), which includes 0.25 inch (6.35 mm) thru lines within each flange. This results in a twist length of exactly $5\lambda_{gL}$, having a rotational smoothness of $18°/\lambda_{gL}$. Our ruggedized 3-D printed counterpart has the same flange-to-flange component length. Any evanescent mode excitation at one port will have significantly decayed over a distance of $5\lambda_{gL}$, avoiding interactions with the other port and, thus, avoiding additional insertion loss.

The 3-D CAD layout for the 90° twist and thru line are shown in the inset of Fig. 2, where L indicates the same total length for both components and the cross-sectional waveguide dimensions are fixed along this length. Simulations are performed using a commercial 3-D full-wave EM simulation software package (High-Frequency Structure Simulator, HFSS). Here, the internal MPRWG walls are represented by annealed copper, having a bulk DC conductivity of 5.8×10^7 S/m. The simulated band-average insertion loss and worst-case return loss for a perfectly matched twist are 0.28 dB and 28.4 dB, respectively, as shown in Fig. 2. Also included in Fig. 2 are the simulation results for a thru line; degraded performance can be inferred by the introduction of the twist.

C. BANDPASS FILTERS

Two 5th order G-band BPFs are designed, having center frequencies of 155 GHz and 175 GHz and associated 3 dB bandwidths of 15.5 GHz and 17.5 GHz, respectively (i.e., both having a 10% fractional bandwidth). Symmetrical diaphragm inductive irises are employed to couple adjacent rectangular TE_{101} mode cavity resonators together. This conventional filter implementation also employs our trough-and-lid assembly solution.

Waveguide BPFs typically use a Chebyshev (Type I) approximation design, due to their steeper transition band roll-off and superior stop-band rejection characteristics when compared to Butterworth approximation filters. However, the former is more sensitive to manufacturing accuracy limitations, as return loss zeros should be precisely distributed across the passband. Indeed, this is confirmed by

the relatively poor passband transmission response of our previous G-band Chebyshev BPF [9]. Therefore, Butterworth approximation designs are employed here, having all return loss zeros located at the center frequency.
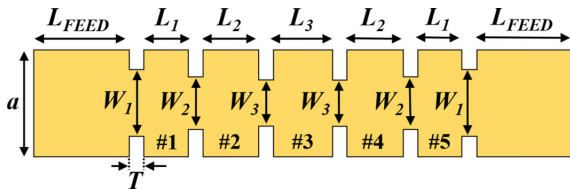

FIGURE 3. Plan view illustration of a symmetrical 5th order waveguide BPF, showing ideal rectangular geometries.

An illustration of a 5th order diaphragm inductive iris-coupled waveguide BPF is shown in Fig. 3, with symmetry. Here, L_{FEED} is the length for both the input and output feed lines and L_i is the length of the ith cavity resonator ($i \in$ [1, 2, 3, 4, 5]). The aperture width of the jth iris is denoted by W_j ($j \in$ [1, 2, 3, 4, 5, 6]), with all irises having thickness $T = 270\ \mu m$. The H-plane a-edge split provides a complete internal plan view of the trough, enabling the detection of visual defects and allowing dimensional characterization. This is not possible with a symmetrical E-plane split or single-block designs, with non-destructive testing.

Our first design step calculates the ideal linear dimensions, using standard textbook filter synthesis [65], with minor tuning performed in HFSS. An arbitrary feed length $L_{FEED} \approx \lambda_{gL}/2$ is used, with respective flange-to-flange lengths of 10.4 mm and 7.4 mm for the 155 GHz and 175 GHz BPFs. The thru lines have the same flange-to-flange lengths, to establish a baseline insertion loss for comparison.
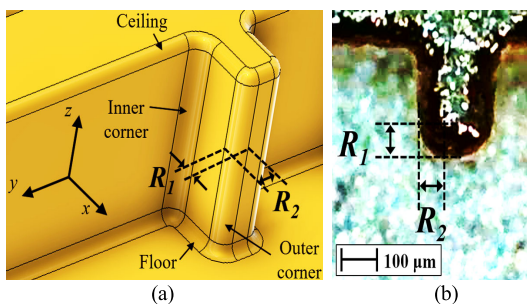

FIGURE 4. Single iris rounding: (a) CAD isometric representation; and (b) 3-D printed and copper electroplated, plan view microphotograph.

Our second design step is to characterize the corner rounding, as illustrated in Fig. 4(a). Rounding at the bottom and top of the trough or iris is referred to here as floor and ceiling rounding, respectively. However, EM simulations have shown that both these types of rounding exhibit a negligible influence on passband performance. Moreover, negligible floor rounding is found in practice, as shown in Fig. 4(b), due to the layer-by-later nature of 3-D printing. However, ceiling rounding is significant, due to erosion during post-print cleaning. As shown in Fig. 4(b), significant ceiling rounding does not reflect the incident light (projected from an elevated position) and is observed as a dark rim.

Only inner and outer iris rounding is considered. The former results from an excess resin residue, due to insufficient post-print cleaning. The latter is mainly due to erosion during post-print cleaning, prior to full UV curing; as well as pixelation and UV light dispersion. Rounding radii are best measured at the mid-point of the internal sidewalls, to avoid any contributions from the floor and ceiling rounding. Iris corner rounding is found to be elliptical, rather than circular, giving two ICR radii per corner (R_1 and R_2), as illustrated in Fig. 4(a) for outer rounding. Similar variables can also be assigned to inner rounding, although their sizes will be approximately similar to the outer rounding. It has been found here, from preliminary printed and plated filter implementations (without any compensation), that the arithmetic mean value for all ICR radii $R \approx 100\ \mu m$. As a result, this single value is used in our rounded BPF designs, as a means of compensation with printing and plating.
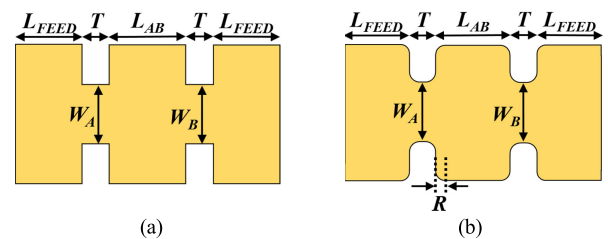

FIGURE 5. Plan view illustration of a single cavity resonator, having two inductive irises: (a) non-rounded; and (b) rounded.

Our final design step is to implement ICR compensation. Figure 5 illustrates the non-rounded and rounded single res-onator geometries used in simulations; the latter employing the Fillet tool in Fusion 360. The cavity has two adjacent inductive irises, with L_{FEED}, L_{AB}, T and $W_{A,B}$ corresponding to the feed length, cavity length, iris thickness and iris aperture widths, respectively. With the rounded case, circular radius R is applied to both irises, effectively increasing the iris width. This results in a 3 dB bandwidth increase, due to an increase in the coupling coefficients [66]. Moreover, the cavity's effective electrical length increases, due to an increase in the effective iris electrical length, resulting in a resonator center frequency down-shift. With every iris corner being rounded by the same amount in the simulations, the full BPF frequency response also has a 3 dB bandwidth increase and a center frequency down-shift.

Simulations are first undertaken with the non-rounded cavity resonator, giving target values for the center frequency and 3 dB bandwidth. Then, with the pre-determined value of R, parametric sweeps of L_{AB} and $W_{A,B}$ are applied to tune the rounded cavity resonator to the fixed target values for center frequency and 3 dB bandwidth from the non-rounded case.

With the symmetrical 5th order BPF, illustrated in Fig. 3, the individual cavity resonators are treated independently, as shown in Fig. 5, with Cavities #1, #5 and #2, #4 being identical. The compensation process starts at the center, with Cavity #3 having two swept variables L_3 and W_3. Then Cavities #2, #4 have their two variables L_2 and W_2

swept, with the previous value of W_3 fixed; this is followed by Cavities #1, #5 having their two variables L_1 and W_1 swept with the previous value of W_2 fixed. Finally, the individual rounded cavity resonators are combined to create the complete rounded BPF for simulation, with minor tuning applied (if required).
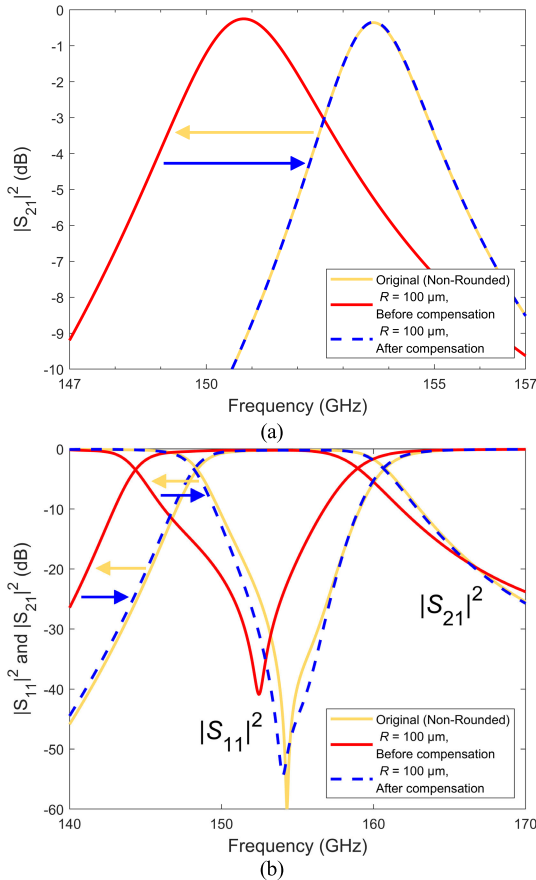
TABLE 4. Non-rounded and compensated linear dimensions for the 155 GHz and 175 GHz BPFs.

Linear Dimensions	$f_0 = 155$ GHz		$f_0 = 175$ GHz	
	Non-rounded (μm)	$R = 100$ μm, Compensated (μm)	Non-rounded (μm)	$R = 100$ μm, Compensated (μm)
L_{FEED}	1849	1873	919	1023
L_1	870	863	672	635
L_2	1093	1082	851	807
L_3	1156	1144	896	851
W_1	1000	979	905	880
W_2	790	746	700	680
W_3	690	645	625	605
T	270	270	270	270

IV. FABRICATION

A. 3-D PRINTING WITH POST-PROCESSING

The low-cost ($230) Elegoo Mars 2 Pro was used for 3-D printing, having a maximum print volume of 80 mm × 129 mm × 160 mm [67]. This model has a 2K monochrome liquid crystal display (LCD) mask, with a 49.4 μm × 50.4 μm pixel size [9]. The Elegoo Water Washable Rapid Resin (Ceramic Grey) provides high accuracy, low shrinkage and can be cleaned with water (i.e., without organic solvents).
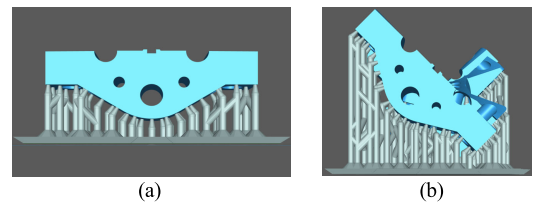

FIGURE 6. ICR compensation simulations applied to the 155 GHz BPF, with yellow and blue arrows indicating frequency shifting due to detuning and compensation, respectively: (a) Cavity #3; and (b) complete BPF.

FIGURE 7. Flange views of print orientations in Chitubox, showing support structures: (a) thru lines and BPFs; and (b) 90° twists.

Figure 6(a) shows the results of ICR compensation when applied to Cavity #3 for the 155 GHz BPF. The yellow and blue arrows indicate the down- and up-shifting due to ICR and its compensation, respectively. It can be seen that, with $R = 100$ μm, ICR causes a center frequency down-shift of 2.0% (3.0 GHz) and a 3 dB bandwidth increase of 40% (1.0 GHz). After compensation, the non-rounded response is almost fully restored. It should be noted that Cavity #3 has the highest loaded Q-factor and, therefore, has the greatest sensitivity to rounding, when compared to the other cavity resonators.

The simulation results for the complete rounded BPF are shown in Fig. 6(b). It can be seen that, with $R = 100$ μm, ICR causes a center frequency down-shift of 1.8% (2.8 GHz) and a 3 dB bandwidth increase of 14.2% (2.2 GHz). After compensation, the non-rounded response is almost fully restored, with the small differences being attributed to the cumulative effect from reconstructing the complete BPF. The final linear dimensions are given in Table 4.

The orientation of each part on the printer's build plate is determined using the Chitubox Basic slicer software, as shown in Fig. 7 [68]. To avoid defects on critical surfaces (e.g., internal waveguide and flange), support material is only attached to non-critical outer surfaces. For the thru lines and BPFs, the H-plane split is kept parallel to the build plate, whereas the 90° twists are rotated by 45° such that the two waveguide ports are at ±45° (to minimize overhang). These orientations are found to optimize dimensional accuracy within the waveguides. Note that anti-aliasing is not applied in Chitubox, as this will increase the levels of corner rounding.

After printing, all parts are post-processed at room temperature to remove all mechanical support structures and uncured resin residue. This is undertaken using the following steps: (i) remove parts from the build plate; (ii) mechanically remove all support structures; (iii) pre-rinse in water; (iv) place in an ultrasonic water bath for 2 minutes; (v) water-jet clean and soft brush trough corners and grooves, to remove

uncured resin residue; (vi) dry with compressed air; and (vii) post-UV cure in natural light for at least 4 hours. Note that using a UV lamp for faster post-curing is avoided, since this can result in warping, shrinkage and layer delamination.

B. METALIZATION

With the commercial copper electroplating process, a thin electroless-plated nickel seed layer is first deposited, followed by a 50 μm thick layer of electroplated copper, corresponding to 283 skin depths at 140 GHz. This guarantees a minimum thickness at corners and edges; < 50 μm thickness can cause underplating. Finally, an anti-tarnishing treatment is applied.

Metalization causes a narrowing of internal waveguide dimensions, which is compensated for in the CAD drawing. Initially, a standard 50 μm deposition process was used. However, the plating thickness was found to be only 35 μm inside the waveguide. This underplating is believed to be the result of having a narrow trough (with higher conduction current density during electroplating). Subsequent waveguides were re-designed to account for the 35 μm thickness within the trough when using the standard 50 μm process.

C. ASSEMBLY

After 3-D printing and electroplating, and prior to full assembly, the 7.4 mm and 10.4 mm thru lines and the 90° twist weigh 4.7 g, 6.6 g and 15.8 g, respectively. The 175 GHz and 155 GHz BPFs are essentially the same weight as the respective 7.4 mm and 10.4 mm thru lines.
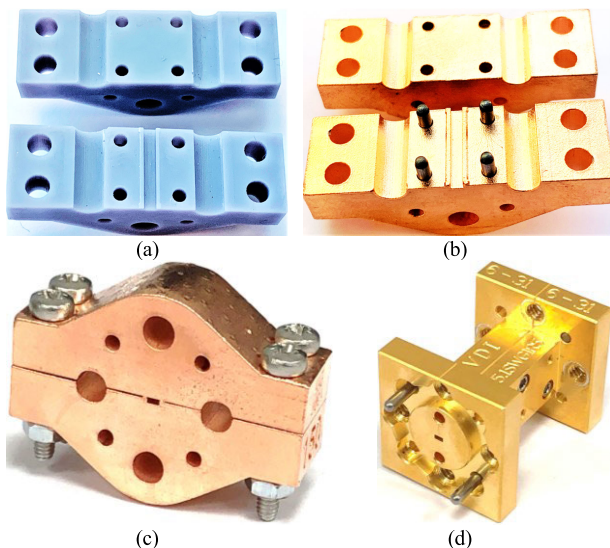

FIGURE 8. WR-5 MPRWG thru lines: (a) disassembled 3-D printed 10.4 mm thru line, before plating; (b) disassembled, after plating, showing stainless steel dowel pins; (c) fully assembled, after plating; and (d) 25.4 mm COTS counterpart from VDI [17].

The disassembled 3-D printed 10.4 mm thru line, before and after electroplating, is shown in Figs. 8(a) and 8(b). Two pairs of stainless steel screws, nuts and washers are used for assembly. Alignment between the two ruggedized parts is further improved by using two pairs of stainless steel

dowel pins, which ensure flat flange interfaces, as shown in Fig. 8(b). The fully assembled 3-D printed 10.4 mm thru line is shown in Fig. 8(c). A 25.4 mm thru line COTS counterpart, from Virginia Diodes Inc. (VDI) [17], is shown in Fig. 8(d), which appears to have a textbook symmetrical E-plane split.
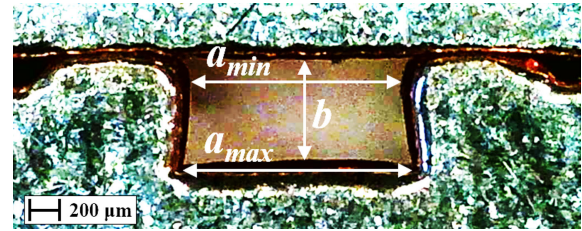

FIGURE 9. Flange view microphotograph of the trough-and-lid assembly for a thru line, showing lips in contact with the flat top part.

The trough-and-lid assembly for a thru line is shown in Fig. 9, where a_{min} and a_{max} refer to the minimum and maximum trough widths, respectively. Overtightening has caused rectangular-to-trapezoidal cross-sectional distortion, with $\sim9°$ of lip bending, shown in Fig. 9. The effect on measured performance will be discussed in Section VI.
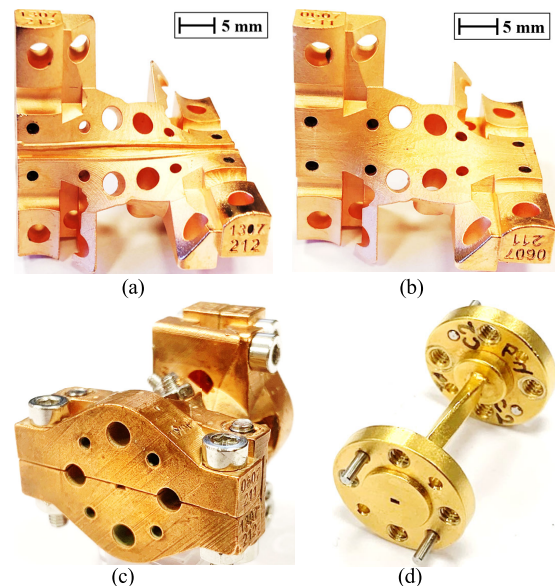

FIGURE 10. WR-5 MPRWG 31.75 mm 90° twists: (a) disassembled 3-D printed and copper electroplated bottom part; (b) disassembled top part; (c) fully assembled; and (d) COTS counterpart from Pasternack [39].

The same assembly approach has also been adopted for the twists. Here, with the longer waveguide length, six pairs of screws, nuts and washers and four pairs of stainless steel dowel pins are used for the assembly of the ruggedized parts. Images of a disassembled and assembled 3-D printed twist, along with its COTS counterpart, are shown in Fig. 10. Unlike the thru lines, it was found that a tight assembly did not introduce significant cross-sectional distortion. This is likely due to the distributed forces being exerted in different directions along the waveguide length. It can be seen in Fig. 10(a) that there are imperfections in the floor of the trough.
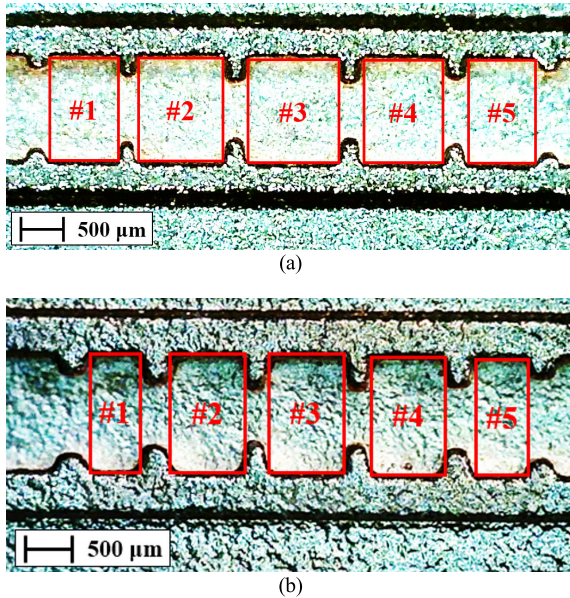
FIGURE 11. Plan view microphotographs of the internal structure for 3-D printed and copper electroplated 5th order Butterworth BPFs, with cavity resonators labelled and feed lengths omitted: (a) $f_0 = 155$ GHz; and (b) $f_0 = 175$ GHz. Red rectangles highlight the peripheries of the cavities.

BPF designs were almost identical to their corresponding thru lines, but with the addition of the irises within the trough. The internal waveguide features for the 155 GHz and 175 GHz BPFs (without feeds) are shown in Fig. 11. Post-assembly cross-sectional distortion was negligible. This is likely due to the irises providing lateral reinforcement.

Note that, while assembly with stainless steel screws, nuts, washers and dowel pins is convenient for prototyping, a possible commercial solution would use conductive epoxy glue, which mitigates against radiation leakage while enabling simpler assembly and weight reduction.

D. COST COMPARISON

Each 3-D printed component costs approximately $0.20 to print, while the additional commercial copper electroplating costs approximately $82 (depending on the total surface area). Table 5 shows a more accurate cost comparison for G-band COTS thru lines and 90° twists, all sourced from the US (Pasternack Enterprises Inc., Fairview Microwave Inc. and Hasco Components Inc.). Prices for G-band BPFs are not included, as these components have bespoke specifications. The cost ratio is defined here as the purchase cost of the COTS component per unit length divided by total manufacturing cost per unit length of our 3-D printed counterpart. It will be seen in Section VI that the measured performance of our 3-D printed twist is commensurate with the Pasternack COTS twist. The cost savings capability of 3-D printing is demonstrated by the little additional cost incurred by the 3-D printed twist in comparison to the thru line.

V. SURFACE ROUGHNESS

A conductor with a rough surface has additional losses, due to localized EM wave scattering from and power dissipation

TABLE 5. Comparative costs (at the time of writing) for G-band thru lines and 90° twists with COTS components and their 3-D printed counterparts. (*costs available online).

Component Type	COTS Manufacturer	Cost ($)*	Length (mm)	Cost per length ($/mm)	Cost ratio	Ref.
Thru Line	Pasternack	456	25.4	18	2.4	[69]
	Fairview	429	25.4	17	2.3	[70]
	Hasco	259	25.4	10	1.4	[71]
	ICL (3-D printed)	78	10.4	8	-	**This work**
90° Twist	Pasternack	735	31.75	23	8.5	[39]
	Fairview	414	31.8	13	4.8	[72]
	Hasco	407	25.4	16	5.9	[73]
	ICL (3-D printed)	86	31.8	3	-	**This work**

within microscopic surface defects [74]. Both become more significant at higher frequencies, as the dimensions of these defects become more significant when compared to the wavelength and classical skin depth, respectively. For example, the authors previously measured the root mean square (RMS) profile roughness $R_q = 1.16$ μm for electroplated copper on an SLA-printed MPRWG [4]. By comparison, the classical skin depths for copper are 0.18 μm and 0.14 μm at 140 GHz and 220 GHz, respectively. As a result, surface roughness is expected to be an important contributor to insertion loss at G-band.

Surface roughness models generally relate either the power dissipated P_{DR} or dissipative attenuation α'_{DR} for rough conductors normalized to smooth conductors (P_{DS} or α'_{DS}), using a frequency-dependent roughness coefficient K [75]:

$$K = P_{DR}/P_{DS} = \alpha'_{DR}/\alpha'_{DS} \qquad (1)$$

Using (1), most models fall into one of two categories: (i) phenomenological models, which fit empirical equations to α'_D measurements; and (ii) physical models, which apply analytical (Maxwell's) equations with boundary conditions set by the specific surface structures. With the former, the most commonly used examples are the Hammerstad-Jensen (HJ) model [75] and the Groiss model [76]. However, their roughness coefficients asymptotically approach $K = 2$ at relatively low frequencies (*ca.* 5 GHz), even with sub-micron values for R_q, making them unsuitable for G-band applications. With the latter, the most commonly used examples are the conventional Hemispherical model [77], which considers hemispherical protrusions on a flat plane, and the Huray model [74], which considers pyramidal protrusions of stacked spheres. The appropriate choice of physical model is dependent on the geometries of the surface defects observed on fabricated components.

Images of the iris sidewalls and the bottom of the MPRWG trough for the plated 155 GHz BPF are shown in Fig. 12, taken using a Zeiss LEO 1450VP scanning electron microscope (SEM). The surface roughness is representative of all plated parts. The main surface defects are approximately
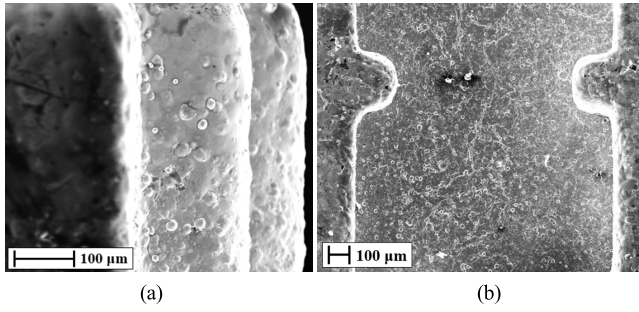
FIGURE 12. SEM images for the 155 GHz BPF: (a) iris sidewalls; and (b) plan view of the bottom of the MPRWG trough and one iris aperture.

hemispherical, suggesting that the Hemispherical model is appropriate. Based on our detailed statistical analysis of the microphotographs in Fig. 12, the average hemispherical radius r_{base} and separation distance between adjacent protrusions d_{peaks} are found to be 3.7 μm and 17 μm, respectively. This corresponds to an effective value of $R_q = 1.41$ μm at the peaks of the hemispheres, which agrees well with our previous measurement of $R_q = 1.16$ μm.

Simulation-based techniques represent another surface roughness model category [78], [79]; these were not considered, as the observed surface defects strongly suggest that the Hemispherical model is appropriate.
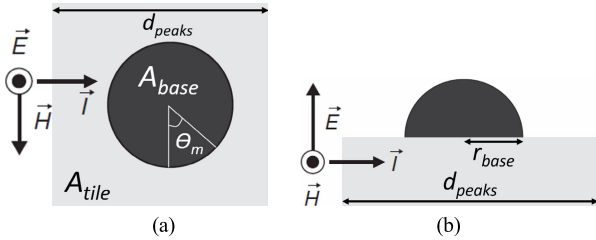

FIGURE 13. The Hemispherical surface roughness model, represented by a single hemispherical protrusion positioned on a flat plane, with incident plane wave propagating parallel to the flat surface: (a) plan view; and (b) side view [80].

Figure 13 illustrates a single cell for the Hemispherical model, which is assumed to extend periodically in the longitudinal and transverse directions, across the entire conductor surface. A transverse electromagnetic (TEM) plane wave is applied, with electric field $\vec{E}$ normal to the flat plane and the magnetic field $\vec{H}$ being tangential, with the direction of propagation from left to right in Fig. 13. The dimensions A_{base} and A_{tile} refer to the areas of the hemisphere base and flat tile, respectively, [77]. These can be related to the average physical dimensions, obtained from SEM images, as:

$$A_{base} = \pi r_{base}^2 \ [\text{m}^2] \tag{2a}$$

$$A_{tile} = d_{peaks}^2 \ [\text{m}^2] \tag{2b}$$

A simplified equation for the Hemispherical model [77] roughness coefficient is:

$$K = \frac{\eta_o}{2R_S} \cdot \frac{\sigma_t}{A_{tile}} + \frac{A_{tile} - A_{base}}{A_{tile}} \tag{3}$$

where η_o and R_S are the intrinsic impedance of free space and classical surface resistance for a smooth conductor (calculated using bulk DC conductivity σ_o), respectively. The total cross-section σ_t, is the sum of the power dissipated and scattered by a conducting sphere positioned in free space divided by the incident flux (power surface density) [81]. Here, the dissipated and scattered fields are solved analytically, with the latter being derived from spherical Bessel functions [81] to give:

$$\sigma_t = \sigma_{dissipated} + \sigma_{scattered} \ [\text{m}^2] \tag{4a}$$

$$\sigma_t = \frac{2\pi}{k_o^2} \sum_1^i \frac{(k_0 r_{base})^{2i+1}}{[(2i-1)!!]^2} \cdot Im\{\alpha_i + \beta_i\} \ [\text{m}^2] \tag{4b}$$

where $\sigma_{dissipated}$ and $\sigma_{scattered}$ are the dissipated and scattered cross-sections, $k_0 = 2\pi/\lambda_0$ is the angular wavenumber, α_i and β_i are dimensionless scattering coefficients and i is a summation term. For $k_0 r_{base} \ll i$, the following long-wavelength approximations are given as [81]:

$$\alpha_i \simeq \frac{k_0 r_{base} - j(i+1)Z_S/\eta_0}{k_0 r_{base} + jiZ_S/\eta_0} \tag{5a}$$

$$\beta_i \simeq \frac{k_0 r_{base} - j(i+1)\eta_0/Z_S}{k_0 r_{base} + ji\eta_0/Z_S} \tag{5b}$$

The conventional Hemispherical model employs only the first term ($i = 1$) and is quoted as being valid up to 30 GHz [77]. However, to provide better accuracy for G-band, σ_t is calculated up to $i = 5$. This is referred to here as the Extended-Hemispherical model.

The conventional Huray model calculates $\sigma_t = \sigma_{dissipated}$, with $\sigma_{scattered}$ being omitted, using a different equation for the roughness coefficient (i.e., not employing (3)). Moreover, instead of using (4b) and any long-wavelength approximations, the 1st order Born approximation for the amplitude of the scattered fields is employed in (4a) with [74]:

$$\sigma_{dissipated} \simeq \frac{3\pi k_0 r_{base}^2 \delta_o}{1 + \frac{\delta_o}{r_{base}} + \frac{1}{2}\left(\frac{\delta_o}{r_{base}}\right)^2} \ [\text{m}^2] \tag{6a}$$

$$\sigma_{scattered} \simeq \frac{10}{3}\pi k_o^4 r_{base}^6 \left[1 + \frac{2}{5} \cdot \frac{\delta_o}{r_{base}}\right] \ [\text{m}^2] \tag{6b}$$

where $\delta_o = 1/\sigma_o R_S$ refers to the classical skin depth of the conductor, calculated using bulk DC conductivity. By including the $\sigma_{scattered}$ term in (6b), giving better accuracy for G-band, and adopting the Hemispherical model roughness coefficient equation in (3), this is referred to here as the Huray-Hemispherical model [74]. To the best of our knowledge, these Extended/Huray-Hemispherical models have not been previously applied to MPRWG applications.

With a perfectly smooth surface, A_{base} and σ_t are both zero, and so $K = 1$. The application of $K > 1$ to EM simulations is introduced in Section VI. Using the values of r_{base} and d_{peaks} obtained from SEM images, the calculated mid-band values are $K(180\ \text{GHz}) = 1.32$ and 1.28 for the Extended- and Huray-Hemispherical models, respectively, with minimal variation across the band. The calculated K

values are multiplied by the calculated/simulated α'_{DS} to obtain α'_{DR}, as given by (1).
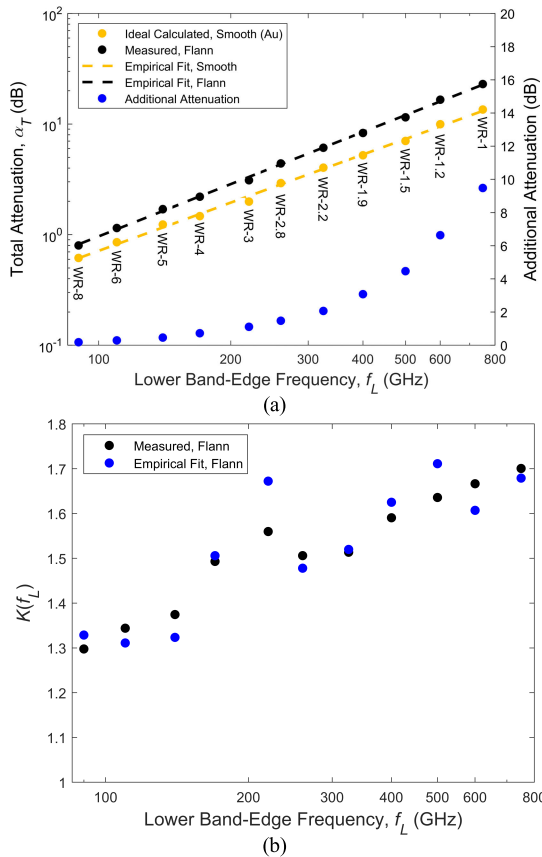

FIGURE 14. Flann submillimeter seamless waveguides: (a) total attenuation measurements, with ideal calculated values and COTS thru line measurements; and (b) effective roughness coefficient K_{eff} (f_L).

An example of a phenomenological model for the roughness coefficient can be seen in Fig. 14. Here, Fig. 14(a) shows the measured total attenuation, $\alpha_{TR} = -10\log_{10}|S_{21}|^2$, for 100 mm long Flann Microwave Ltd COTS submillimeter seamless MPRWG thru lines [11], previously introduced in Section II.A. Their current catalog covers 11 waveguide bands, ranging from WR-8 (with $f_L = 90$ GHz) to WR-1 (with $f_L = 750$ GHz). A close fit (derived empirically) to the measurements is found with $\alpha_{TR} \cong 7.1 \times 10^{-4} \cdot f_L \text{(GHz)}^{1.5669}$, having a coefficient of determination $R^2 = 0.9986$, shown in Fig. 14(a). In addition, Fig. 14(a) also includes the dissipative attenuation for 100 mm long smooth thru lines α_{DS}, calculated at f_L. Here, standard textbook equations are used (e.g., Pozar [82]), given in Section VI, with bulk DC conductivity for gold (since all the thru lines are gold-plated). A close fit (derived empirically) to the calculated results is found with $\alpha_{DS} \cong 9.2 \times 10^{-4} \cdot f_L \text{(GHz)}^{1.4452}$, having a coefficient of determination $R^2 = 0.9980$, shown in Fig. 14(a).

For these COTS thru lines, the effective roughness coefficients $K_{eff}(f_L) = \alpha_{TR}/\alpha_{DS}$, with results given in Fig. 14(b). Using the previously derived empirical fits, effective $K_{eff}(f_L) \sim 0.77 \cdot f_L \text{(GHz)}^{0.1217}$. These values will be

an overestimation, as the total attenuation is increased by the contribution from the wave impedance mismatch reflection.

VI. MEASUREMENTS

Scattering (S-)parameter measurements were undertaken at the U.K.'s National Physical Laboratory, using their Keysight Technologies PNA-X N5247B vector network analyzer (VNA) [83], with VDI WR-5.1 frequency extender heads [84]. Thru-Reflect-Line (TRL) calibration was undertaken prior to measurements, with reference planes at the VNA frequency extension heads. The two-port device under test (DUT) is assembled and placed between the two measurement reference planes, as shown in Fig. 15.
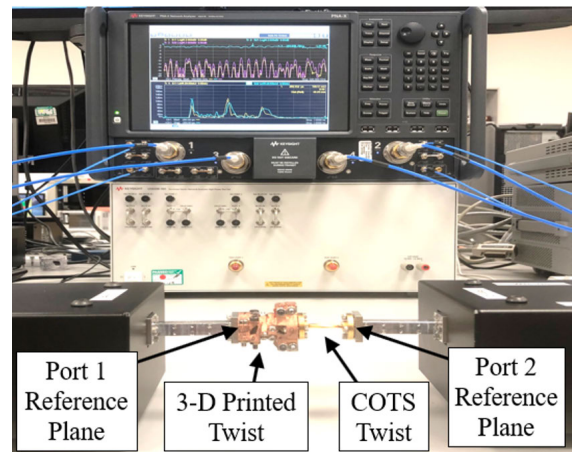

FIGURE 15. Two-port waveguide measurement setup, with VNA screen displaying the frequency-domain response (top panel) and time-domain response (bottom panel). The DUT here is a 3-D printed 90° twist connected to a COTS 90° twist (i.e., Cascade #1).

A. THRU LINES

The 7.4 mm and 10.4 mm 3-D printed thru lines are measured. In addition, two VDI WR-5 thru line counterparts, of lengths 25.4 mm and 50.8 mm, are included for comparison. The measured aperture dimensions [a_{min}, a_{max}, b] for the 3-D printed thru lines are [1,010 μm, 1,320 μm, 680 μm] and [1,000 μm, 1,290 μm, 690 μm] for the 7.4 mm and 10.4 mm thru lines, respectively. The COTS thru lines are machined from aluminium alloy 6061-T6, with quoted cross-sectional aperture dimension being ideal [1,295 μm, 1,295 μm, 647.5 μm] [85]. Gold (with bulk DC conductivity of 4.1×10^7 S/m) is used for all COTS thru line theoretical calculations and EM simulations, since the machined parts are gold plated. Copper is used for all 3-D printed counterparts. All COTS components are assumed to be smooth internally. Moreover, all responses that are referred to in this paper as 'EM simulated' adopt the ideal dimensions in HFSS.

Figure 16 shows the reflection measurements for all thru lines across G-band. The S_{11} and S_{22} responses are in good agreement, indicating a similar wave impedance mismatch at both ports. The worst-case return loss is 14.9 dB and 14.1 dB for the 7.4 mm and 10.4 mm 3-D printed thru lines,
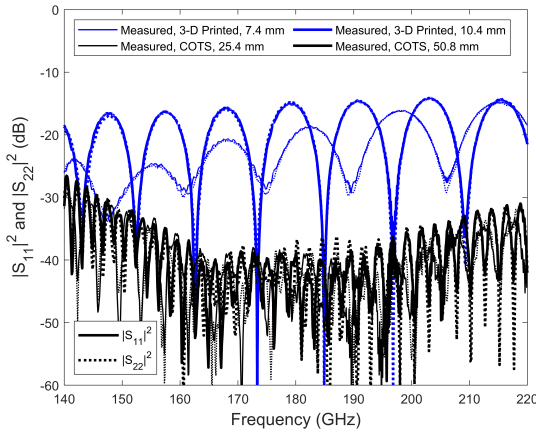
FIGURE 16. Reflection measurements for 3-D printed and COTS thru lines.

respectively. In comparison, they are 27.8 dB and 26.5 dB for the 25.4 mm and 50.8 mm COTS thru lines, respectively. Poor return loss is primarily the result of aperture size and spatial orientation discrepancies at the flange interfaces between the waveguide extender heads (defining the calibrated reference planes) and the DUT. This is exacerbated with 3-D printed thru lines, due to four factors: (i) poorer dimensional accuracy of rectangular apertures; (ii) rounded edges and corners; (iii) rectangular-to-trapezoidal cross-sectional distortion, due to lip bending; and (iv) 3-D misalignment between extender heads and DUT apertures. In comparison, the COTS thru lines exhibit high dimensional accuracy in all aspects.

Nevertheless, the current results compare favorably to those from the previously reported G-band thru line [3], which had a worst-case return loss of 6 dB. This is due to misalignment between parts, associated with the traditional symmetrical E-plane split block approach, being avoided.

Fabry-Pérot ripples are evident in the frequency responses, caused by wave impedance mismatches located at both ports. These have frequency period Δf, correspond to standing-wave reflections between two spatial boundaries that are separated by waveguide length $L \approx v_g(180\,\text{GHz})/\Delta f$, where $v_g(180\,\text{GHz}) = 2.30 \times 10^8$ m/s is the theoretical mid-band group velocity of the waveguide. With $\Delta f = 29.8$, 22.3 GHz, the extracted value for $L \approx 7.7$, 10.3 mm, corresponding to the exact length $L = 7.4$, 10.4 mm between ports.

The ideal textbook transmittance (which assumes perfect wave impedance matching) and the corresponding insertion loss $IL|_{Ideal}$ for an air-filled MPRWG is given by:

$$|S_{21}|^2 = e^{-2\alpha_C L} \tag{7}$$

$$IL|_{Ideal} = 8.686\,\alpha_C L \text{ [dB]} \tag{8}$$

$$\alpha_C = \frac{R_S}{\eta_0} \cdot \frac{2\pi^2 b + a^3 k_o^2}{a^3 b \beta k_0} \text{ [Np/m]} \tag{9}$$

where S_{21}, α_C, L, λ_g and $\beta = 2\pi/\lambda_g$ are the forward voltage-wave transmission coefficient, attenuation constant associated with the smooth conductor [82], waveguide length, guided wavelength and phase constant, respectively.

Total power attenuation $\alpha_T = \alpha_M + L\alpha'_D = -10\log_{10}$ $|S_{21}|^2$ [dB] is equal to insertion loss, where α_M represents the contribution to the total attenuation due to the wave impedance mismatch reflection at the input port and α'_D represents the dissipative attenuation per unit length due to ohmic losses [4], [86]:

$$\alpha_M = -10\,\log_{10}(1 - |S_{11}|^2) \text{ [dB]} \tag{10}$$

$$\alpha'_D = -\frac{10}{L}\log_{10}\left(\frac{|S_{21}|^2}{1 - |S_{11}|^2}\right) \text{ [dB/m]} \tag{11}$$

where S_{11} is the input voltage-wave reflection coefficient. It should be noted that (10) and (11) assume a DUT that is passive, reciprocal, symmetrical and homogeneous. Since α_M does not contribute to the intrinsic transmission loss performance, only α'_D will be considered here. As a result, (11) represents the ratio of available power into the DUT to the transmitted power out of the DUT, divided by the physical length of the DUT.

The ideal calculated dissipative attenuation $\alpha'_D|_{Ideal}$, with ideal cross-sectional dimensions to give perfect wave impedance matching (i.e., $|S_{11}| = 0$), can be calculated by substituting (7) into (11):

$$\alpha'_D|_{Ideal} = -\frac{IL|_{Ideal}}{L} = 8.686\,\alpha_C \text{ [dB/m]} \tag{12}$$

Therefore, $\alpha'_D|_{Ideal}$ corresponds to the attenuation constant, given by (9), converted from Np/m to dB/m. For resonators, dB/λ_g is a more useful unit, obtained simply by multiplying (11) and (12) by λ_g.
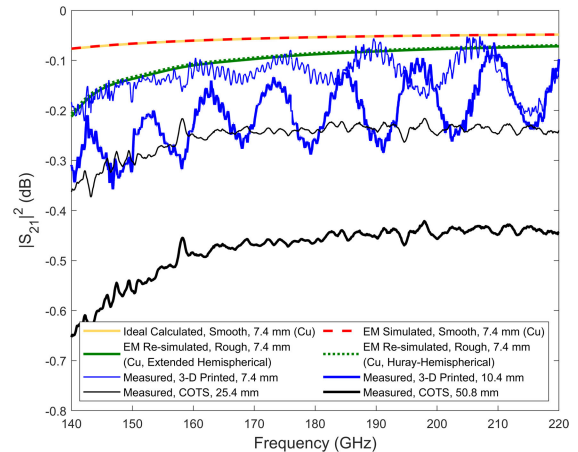

FIGURE 17. Transmission results for the 3-D printed and COTS thru lines.

Figure 17 shows transmission measurements across G-band, as well as the ideal calculated, EM simulated and EM re-simulated responses for a 7.4 mm thru line. All responses that are referred to in this paper as 'EM re-simulated' adopt measured dimensions in HFSS, giving a more accurate characterization of the real component. For example, here, the measured effective mean aperture width $a_{mean} = (a_{min} + a_{max})/2 \cong 1,150\,\mu$m is applied to account

for rectangular-to-trapezoidal cross-sectional distortion. The re-simulated S-parameters are then used to calculate α'_{DS}. In addition, surface roughness losses are included, using the Extended/Huray-Hemispherical model $K(180$ GHz$)$ values calculated previously. The results match closely with the measured data for the 7.4 mm thru line. With the Fabry-Pérot ripples, observed in both reflection and transmission frequency responses, the peaks in the transmission responses (corresponding to the troughs in the reflection responses) approach the EM re-simulated curves.
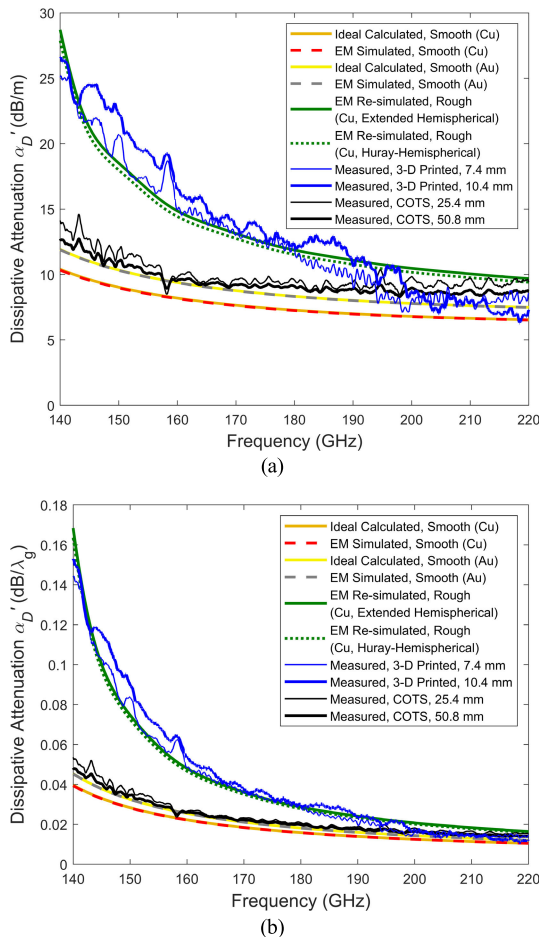

FIGURE 18. Dissipative attenuation for the 3-D printed and COTS thru lines: (a) per meter; and (b) per guided wavelength.

Figure 18 shows the calculated, EM simulated, measured and EM re-simulated α'_D across G-band. Both EM simulated responses are in good agreement with the ideal calculated results, with both modelling scenarios having smooth rectangular walls and perfect wave impedance matching. The measured α'_D, averaged across G-band, is 12.7 dB/m (0.032 dB/λ_g) and 13.7 dB/m (0.035 dB/λ_g) for the 7.4 mm and 10.4 mm 3-D printed thru lines, respectively. In comparison, these measurements are 9.9 dB/m (0.024 dB/λ_g) and 9.4 dB/m (0.022 dB/λ_g) for the 25.4 mm and 50.8 mm COTS thru lines, respectively, comparing well with both ideal calculated and EM simulated results.

With reference to Fig. 18, between *ca.* 200 and 220 GHz, the 3-D printed and COTS thru line performances are commensurate.

EM re-simulations agree closely with the measurements, with effective mean aperture width $a_{mean} \cong 1,150\,\mu$m and the Extended/Huray-Hemispherical model $K(180$ GHz$)$ values being applied. Clearly, the degraded performance for the 3-D printed thru lines below *ca.* 200 GHz can be mainly attributed to the rectangular-to-trapezoidal cross-sectional distortion, with surface roughness adding approximately 2-3 dB/m of additional attenuation across G-band. The narrower effective mean aperture width shifts the TE$_{10}$ mode cutoff frequency from 116 GHz up to 130 GHz, dramatically increasing the attenuation at the lower band edge frequency for G-band. It is worth noting that detailed re-simulations were also undertaken with a trapezoidal cross-section, using measured values for a_{min} and a_{max}, with very similar results to the narrowed rectangular cross-section.

In comparison, our previously reported 3-D printed thru line exhibits an average α'_D of 59 dB/m at G-band [3]. D- and J-band metal-based MLS 3-D printed 50 mm thru lines reported by Zhang and Zirath exhibit an average α'_D of 19 dB/m and 120 dB/m, respectively [12]. Table 1 shows that our current results compare favorably with all 3-D printed D-band thru lines, and are even commensurate with some 3-D printed W-band thru lines, despite having a higher theoretical minimum attenuation due to the smaller aperture dimensions. This provides a robust proof-of-concept for the split-block trough-and-lid assembly.

Time-domain reflectometry (TDR) is a very sensitive tool for detecting impedance mismatches, with its transient responses, which may not be easily seen from steady-state frequency-domain responses. As such, TDR is useful for determining the quality of flange-to-flange wave impedance matching, at port-to-DUT and inter-component interconnects, and for performing a non-invasive test for physical deformation and surface defects within MPRWGs.

Emulated TDR ($|S_{11}|$ and $|S_{22}|$) measurements have been undertaken for the 3-D printed thru lines. Within the VNA, a discrete inverse Fourier transform is applied to the frequency-domain return loss responses (S_{11} and S_{22}). Ideally, this is mathematically equivalent to launching a unit impulse into the DUT and measuring the corresponding reflected response [87]. The resulting TDR response is a series of return pulses, each corresponding to a discrete wave impedance discontinuity. A Kaiser-Bessel window function (with $\beta_K = 6$, which closely approximates a Hanning window function) is applied to the frequency-domain measurements, across G-band with 5,001 data points, before undertaking the inverse Fourier transform using the PNA-X Band Pass Impulse transform mode. Note that, for a band-pass frequency-domain operation having an ideal rectangular (also referred to as 'boxcar', 'top hat' or 'brick-wall') filtering function with a 3 dB bandwidth BW, the corresponding full-width at half-maximum (FWHM) values of the 'synthetic-pulse' for the time-domain impulse response

is $t_{\text{FWHM,R}} = 1.2/BW = 15$ ps, with G-band having $BW = 80$ GHz [87]. Frequency-domain Kaiser-Bessel ($\beta_K = 6$) and Hanning window functions have impulse widths of $t_{\text{FWHM,K}} = 1.63 \times t_{\text{FWHM,R}} = 1.96/BW = 24.4$ ps [87] and $t_{\text{FWHM,H}} = 2/BW = 25$ ps, respectively [88]. From observation, the arithmetic mean reflected impulse width for the EM (re-)simulated and measured TDR data is ≈ 24 ps.

The extracted physical distance d along a thru line between any two points on a TDR trace is given by [87]:

$$d \simeq v_g \Delta t / 2 \quad [\text{m}] \tag{13}$$

where Δt refers to the round-trip time difference between any two points on the trace. The two-port differential-phase group delay $\tau_g = d/v_g \simeq \Delta t/2$. For example, between the two main reflection pulse peaks, Δt should correspond to twice the flange-to-flange length L. Using (13), with $v_g(180 \text{ GHz}) = 2.07 \times 10^8$ m/s calculated using $a \rightarrow a_{mean}$, the second pulse is predicted to arrive at $\sim$72 ps and $\sim$101 ps for the 7.4 mm and 10.4 mm 3-D printed thru lines, respectively.

Emulated TDR $|S_{11}|$ measurements can also be created from frequency-domain EM (re-)simulations, by importing a Touchstone data file into AWR's Microwave Office® (MWO). Here, |TDR_BPI(1,1,0,10,4,0)| calculates the time-domain, Band-Pass Impulse (BPI) response for a linear, time-invariant network. In addition, MWO can emulate TDR measurements from simple circuit elements; as shown in Fig. 19(a) with $a \rightarrow a_{mean}$. Re-simulations apply $K(180 \text{ GHz}) = 1.32$ and 1.28 to give effective bulk DC conductivity values for rough copper of 3.34×10^7 S/m and 3.54×10^7 S/m; these, in turn, give the corresponding MWO circuit simulator 'metal bulk resistivity normalized to copper' values (Rho) of 1.737 and 1.638. The results from both the Extended and Huray-Hemispherical roughness models are almost identical, so only the former is shown.

In order to match with PNA-X TDR measurements, MWO must employ a Hanning window, with a Time Resolution Factor of 10 (to apply sufficient zero-padding in the frequency-domain to increase the time resolution) and an amplitude scaling factor of $\times 2$ (to account for the one-sided frequency-domain spectrum).

It can be shown that, for normal passive homogeneous/uniform media (e.g., material samples or guided-wave structures under test) of infinite thickness/length, the peak of the 'synthetic-pulse' from the magnitude of the input voltage-wave reflection coefficient ($|S_{11}|$) TDR trace can be given by:

$$|\rho_o|_{Peak,R} = \frac{Z - Z_0}{Z + Z_0} \tag{14}$$

where subscript 'R' refers to the use of the rectangular frequency-domain window function, ρ_o is the zeroth-order electric-field wave reflection coefficient, Z is the intrinsic impedance for a material sample or characteristic/wave impedance for a transmission line/waveguide under test and Z_0 is the reference impedance; both impedances must be dispersionless. For a Hanning frequency-domain window
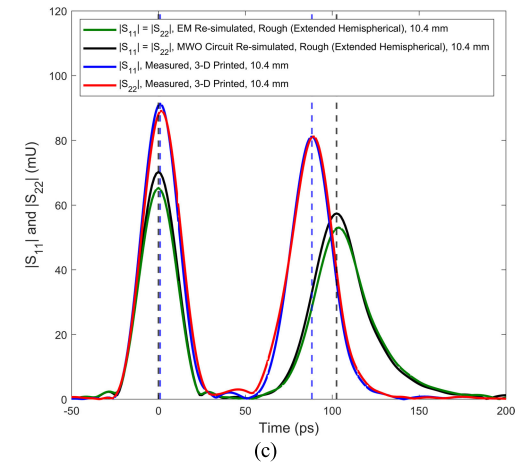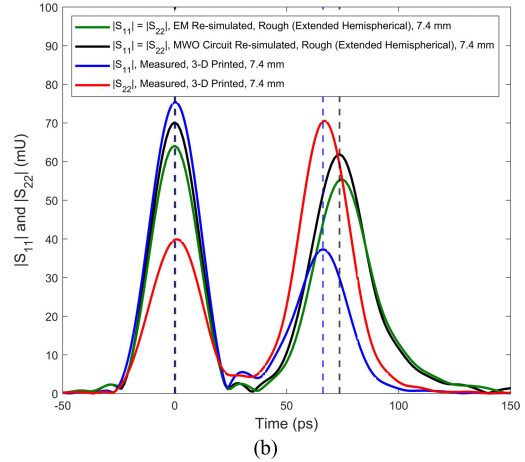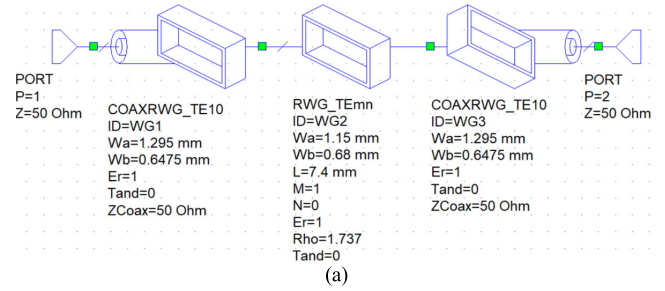

(a)

(b)

(c)

FIGURE 19. Emulated TDR re-simulations and measurements for the 3-D printed thru lines: (a) MWO re-simulated setup for the reduced width 7.4 mm thru line; (b) 7.4 mm thru line traces; and (c) 10.4 mm thru line traces.

function, having subscript 'H', the peak is given by:

$$|\rho_o|_{Peak,H} = \frac{|\rho_o|_{Peak,R}}{2} \tag{15}$$

With a medium of finite thickness/length, two dominant peaks will be seen. Given dispersionless impedances, the first peak is given by the following close approximation:

$$|\rho_o|_{1st \ Peak,R} \cong \frac{Z - Z_0}{Z + Z_0} \tag{16}$$

For an ideal (lossless and dispersionless) medium it can be shown, using a simple heuristic engineering approach [89],

that the second peak is given by the following approximation:

$$|\rho_o|_{2nd\ Peak,H} \simeq \frac{\left(1 - |\rho_o|^2_{1stPeak,R}\right) \cdot |\rho_o|_{1st\ Peak,R}}{2} \quad (17)$$

Equations (14)-(17) are quantitative for lossless and non-dispersive media. However, since waveguides are inherently highly frequency dispersive [90], (14)-(17) can only predict qualitative values, being of the same order of magnitude.

With reference to Fig. 19(b) and 19(c), the straight vertical blue and black dashed lines indicate the timings of reflected pulse peaks from the measured S_{11} (blue trace) and MWO circuit re-simulation $|S_{11}| = |S_{22}|$ (black trace), respectively. The second reflected pulses for the respective 7.4 mm and 10.4 mm 3-D printed thru lines arrive at 74 ps and 104 ps in EM re-simulations and at 73 ps and 102 ps in MWO circuit re-simulations. There is good agreement between the re-simulated values and those previously calculated ($\sim$72 ps and $\sim$101 ps, respectively). However, as shown in Fig. 19, there is a slight discrepancy with the measured results, as the second pulses arrive at 67 ps and 92 ps for the 7.4 mm and 10.4 mm 3-D printed thru lines, respectively. This is believed to be mainly due to mechanical compression of the copper-plated polymer-based thru lines (in the longitudinal direction) with our measurement setup. As a result, from both MWO re-simulations and (13), the respective reduction in lengths are believed to be approximately 0.5 mm (6.8%) and 0.9 mm (9.1%).

Figure 19 qualitatively shows the measured levels of wave impedance mismatching at both ports. From Fig. 19(b) and 19(c), the two dominant peaks are evident. The first peak in $|S_{11}|$ represents the wave impedance mismatch reflection from the unit impulse incident at Port 1 and the second peak corresponds to the reflection at Port 2. Similarly, the first peak in $|S_{22}|$ represents the wave impedance mismatch reflection from the unit impulse incident at Port 2 and the second peak corresponds to the reflection at Port 1. As a useful reference, where there is an equal wave impedance mismatch at both ports, the MWO re-simulations results show that the second peak will be lower than the first, mainly due to the product of the two complex Fresnel transmission coefficients at the incident port being less than unity. From this simulation benchmark, we can establish which port has the worst wave impedance mismatch. For example, with reference to Fig. 19(b), the 7.4 mm thru line has the worse wave impedance mismatch at Port 1, when compared to Port 2. Conversely, with reference to Fig. 19(c), the 10.4 mm thru line has the worse wave impedance mismatch at Port 2, when compared to Port 1.

B. 90° TWISTS

Quantitative two-port measurements of a 90° twist require one of the frequency extender heads to be rotated by 90°. However, at such high millimeter-wave frequencies, the resulting phase mismatch in the associated feed coaxial cable could introduce a significant post-calibration measurement error. Instead, two-port measurements were undertaken by cascading the DUT with another 90° twist, giving a qualitative performance for the 3-D printed twist. As an alternative, quantitative one-port measurements were undertaken by connecting one end of a 90° twist to the Port 1 frequency extender head, with the other end connected to a high quality commercial VDI wave impedance matched-load termination.

Three components are used in the following measurements: the 3-D printed 90° twist and two brand-new commercial 90° twists (referred to here as COTS #1 and COTS #2). The mean measured aperture dimensions $[a, b]$ for these three twists are [1,270 μm, 580 μm], [1,250 μm, 720 μm] and [1,260 μm, 710 μm], respectively, at both ends. Clearly, none of the three components meet the WM-1295 standard of $[a, b] = $ [1,295 μm, 647.5 μm], with the 3-D printed twist having a better dimensional match when compared to COTS #1. Moreover, COTS #1 and COTS #2 have very similar dimensions, while COTS #2 was found to have a visible aperture defect at one of its flanges.
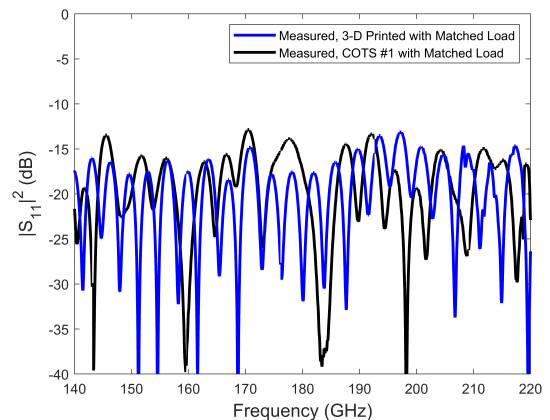

FIGURE 20. One-port reflection measurements for the 3-D printed and COTS #1 twists (terminated with a wave impedance matched load).

Figure 20 shows one-port reflection measurements across G-band for the individual 3-D printed and COTS #1 twists, connected to a wave impedance matched load termination. The COTS #2 twist was not included here, as its flange aperture defect results in poorer reflection measurements when compared to those from the COTS #1 twist. Clearly, our 3-D printed twist has measured results that are commensurate with its brand-new commercial counterpart.

Ideally, without any twist, all the incident power at the commercial wave impedance matched load will be dissipated, resulting in a zero reflection coefficient at this termination. With the twist inserted, the measured reflectance $|S_{11}|^2$ will then represent the reflection response of the individual twist. The worst-case return loss across G-band is 13.2 dB for the 3-D printed 90° twist, while that for the COTS #1 twist is 12.9 dB. The return loss for the 3-D printed twist is generally greater than 15 dB across G-band and commensurate with that for the COTS #1 twist.

For two-port measurements, two cascade combinations were employed: (i) the 3-D printed twist (at Port 1) connected

to COTS #1 (at Port 2), and (ii) COTS #1 (at Port 1) connected to COTS #2 (at Port 2). These shall be referred to here as Cascades #1 and #2, respectively. As the COTS twists are manufactured from gold-plated oxygen-free hard copper [39], associated theoretical calculations and EM (re-)simulations are undertaken using the bulk DC conductivity of gold.
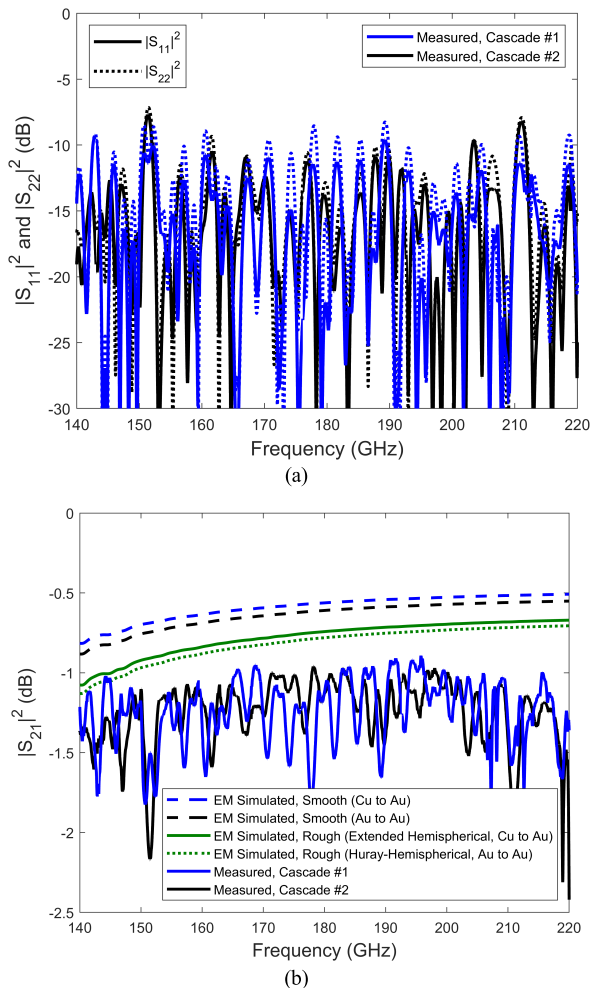

FIGURE 21. EM simulations and measurements for Cascades #1 and #2: (a) reflection; and (b) transmission.

Figure 21(a) shows two-port reflection measurements across G-band for Cascades #1 and #2. Note that, since Cascade #1 is not symmetrical, the S_{11} and S_{22} responses are not identical. The worst-case return loss across G-band is 8.3 dB and 7.2 dB for Cascades #1 and #2, respectively. The 1.1 dB improvement in the worst-case return loss with Cascade #1 can be attributed to the aperture dimensions of the 3-D printed twist being closer to the ideal dimensions, when compared to that for COTS #1 or #2. The poor return loss is the result of three wave impedance mismatches (i.e., at both port flanges and the inter-twist flange interfaces). The Fabry-Pérot ripples in the frequency responses are characteristic of multi-stage reflections.

Figure 21(b) shows two-port transmission measurements for Cascades #1 and #2, across G-band, demonstrating an average insertion loss of 1.24 dB for both cascade scenarios. The qualitative average insertion loss for a single twist is approximately 0.62 dB, given that all twists have similar return loss performances. This suggests a commensurate insertion loss performance between the 3-D printed twist and the COTS counterparts.

The EM simulated transmission responses for two ideal cascaded twists (having perfect wave impedance matching) exhibit significantly lower loss when compared to Cascades #1 and #2. When surface roughness losses are applied, using the Extended/Huray-Hemispherical model $K(180\text{ GHz})$ values, the results are closer to our measurements. However, there is still a significant discrepancy due to the 3-D printed-to-COTS inter-twist mismatch (also found with Cascade #2). Moreover, any intra-waveguide defects, which could be introduced by the respective manufacturing techniques of either twist, may cause significant reflections. For example, within the 3-D printed twist, this would be associated with layer-by-layer defects due to changing printing orientation and by defects seen in Fig. 10(a).

It should be noted that α'_D cannot be investigated with Cascades #1 and #2. This is because (11) is no longer valid, as the wave impedance mismatch reflections from the 3-D printed-to-COTS #1 twist flange interface and intra-waveguide defects result in a non-homogeneous DUT.

Using the mean measured aperture widths of $a = 1.27$ mm and 1.25 mm for the single 3-D printed and COTS #1 twists, respectively, the corresponding calculated mid-band group velocities are $v_g(180\text{ GHz}) = 2.26 \times 10^8$ and 2.24×10^8 m/s. By applying these to (13), the respective second pulses are predicted to arrive at 281 ps and 284 ps, respectively. With Cascade #1, the time of the second pulse for $|S_{11}|$ is equal to that for the one-port 3-D printed twist, with the second pulse for $|S_{22}|$ corresponding to that for one-port COTS #1 twist. The third pulse is predicted to arrive at $281 + 284 = 565$ ps, with both $|S_{11}|$ and $|S_{22}|$ responses.

Figure 22(a) shows one-port TDR traces for the 3-D printed and COTS #1 twists, with Fig. 22(b) showing two-port TDR traces for Cascade #1. VNA measurements and EM re-simulations (with only the Extended-Hemispherical model shown) are given. In Fig. 22(a), two major reflections are observed, corresponding to the interface flanges at the measurement port and at the matched load. In Fig. 22(b), three major reflections are observed, corresponding to the flange interfaces at the two measurement ports and between the twists.

With reference to Fig. 22(a) and 22(b), the second reflected pulses arrive at 267 ps and 281 ps in the measurements and at 281 ps and 283 ps in the EM re-simulations, for the 3-D printed and COTS #1 twists, respectively. It should be noted that the previously calculated single-twist arrival time predictions are for a 31.75 mm thru line, using (13), which gives almost identical values with EM re-simulations for the 31.75 mm long twists. With reference to Fig. 22(b),
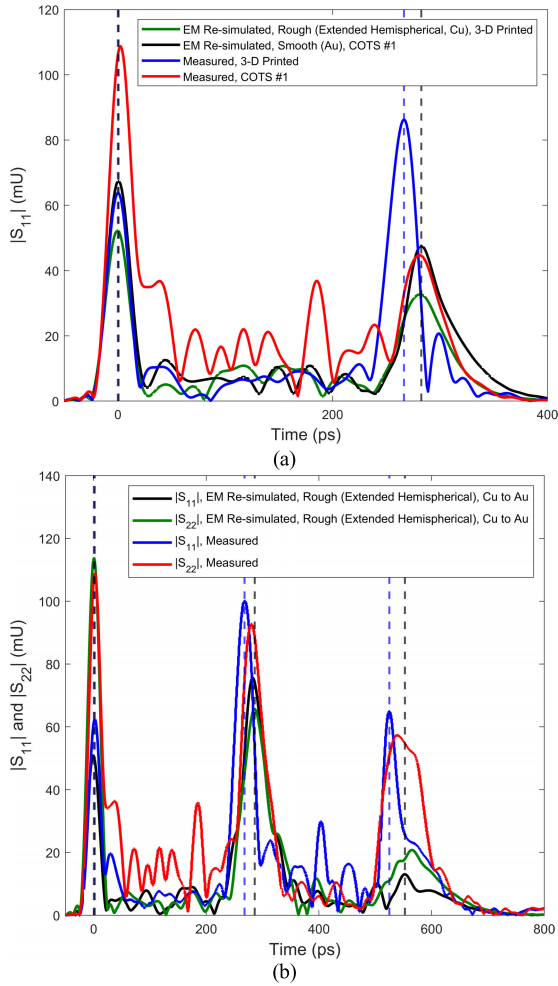
FIGURE 22. TDR measurements and EM re-simulations: (a) one-port for the 3-D printed and COTS #1 twists terminated with a VDI matched load; and (b) two-port for Cascade #1.

the third reflected pulses arrive at 525 ps and 539 ps for the corresponding S_{11} and S_{22} measurements and at 553 ps and 565 ps in the EM re-simulations.

The slight discrepancy between measured and calculated/re-simulated results is due to mechanical compression of the 3-D printed twist in the longitudinal direction with our measurement setup. The reduction in the 3-D printed twist lengths, calculated using (13) with the timings of the second pulses in Fig. 22(a) and 22(b), is approximately 1.6 mm (5.0%).

Overall, the 3-D printed twist has a better wave impedance match, when compared to COTS #1. With reference to Fig. 22(a), it can be seen that the 3-D printed twist has a worse wave impedance mismatch at Port 2, when compared to Port 1. Conversely, COTS #1 has a worse wave impedance mismatch at Port 1, when compared to Port 2.

Between the main reflections, smaller pulses can also be seen in Fig. 22, both in the measurements and re-simulations. The latter are consistent in magnitude with both the 3-D printed and COTS #1 twists. These are believed to be due to distributed reflections from the twisting transition.

Moreover, these re-simulated smaller pulse amplitudes agree with those measured for the 3-D printed twist. However, the commercial twist exhibits significant smaller pulses, which are much greater in magnitude than those predicted through re-simulations. Since internal discontinuities are not included in the re-simulations, and also because of the short time intervals between the smaller pulses, it is believed that they are due to internal defects seen in the measured results. These may have occurred due to forced mechanical rotation during manufacture. Note that this cannot be verified without destructive visual inspection.
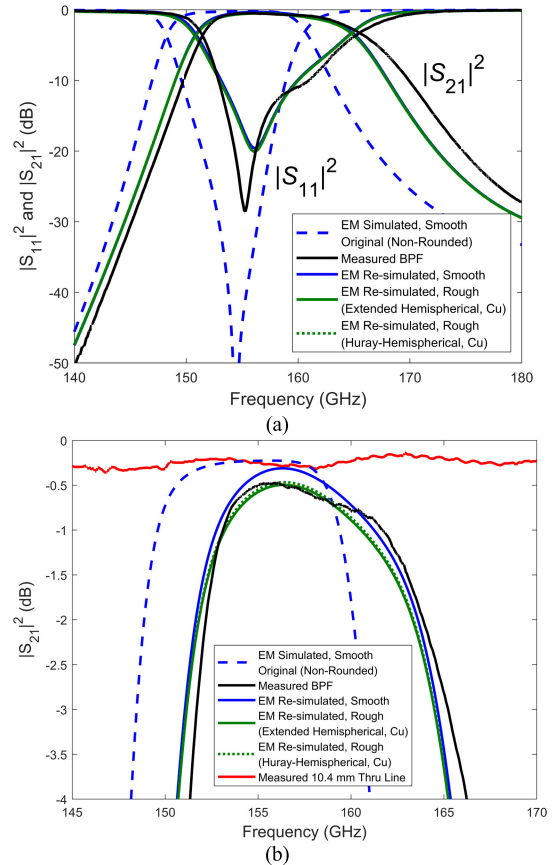

FIGURE 23. EM simulated, measured and EM re-simulated two-port S-parameter responses for the 10.4 mm long 155 GHz BPF, with ICR compensation applied: (a) G-band responses; and (b) close-up passband transmission responses, with the 10.4 mm reference thru line included.

C. BANDPASS FILTERS

Figure 23 shows the S-parameter responses for the 155 GHz BPF, showing EM simulated, measured and EM re-simulated results (i.e., using measured dimensions and iris corner rounding). As with the thru lines and twists, surface roughness is included in the EM re-simulations, with the Extended- and Huray-Hemispherical models; the latter not being visible in Fig. 23(a). The measured and re-simulated responses agree well, suggesting that the measured dimensions are accurate.

It can be seen from Fig. 23 that the BPF almost preserves the typical Butterworth approximation, having the characteristic mid-band single return loss zero. In contrast, our

previously published G-band 5th order Chebyshev filter [9] lost its characteristic return loss zero passband distribution, mainly due to not incorporating ICR compensation.

At the center frequency, the measured insertion losses for this 10.4 mm long BPF and reference 10.4 mm thru line are 0.47 dB and 0.24 dB, respectively, giving a minimum discrepancy of only 0.23 dB at 155 GHz. With both the BPF and thru line there is a good impedance match at 155 GHz, with return losses at 20 dB. It is evident that surface roughness and resonator detuning (due to manufacturing inaccuracy) are the main contributors to insertion loss (i.e., there is insignificant radiation leakage).

There is a slight center frequency up-shift of 2.3% (3.6 GHz) and an 8.4% (1.3 GHz) decrease in 3 dB bandwidth, increasing Q_L from the target value of 10 to the measured value of 11.2. Passband frequency shifting can be explained by measuring the linear dimensions and ICR. The former were found to be a good fit to its predicted compensation values. However, the measured average ICR radius is 75 μm, compared to the predicted compensation value of $R = 100$ μm. Since ICR compensation results in a center frequency up-shift and a 3 dB bandwidth narrowing, this suggests that over-compensation has occurred.
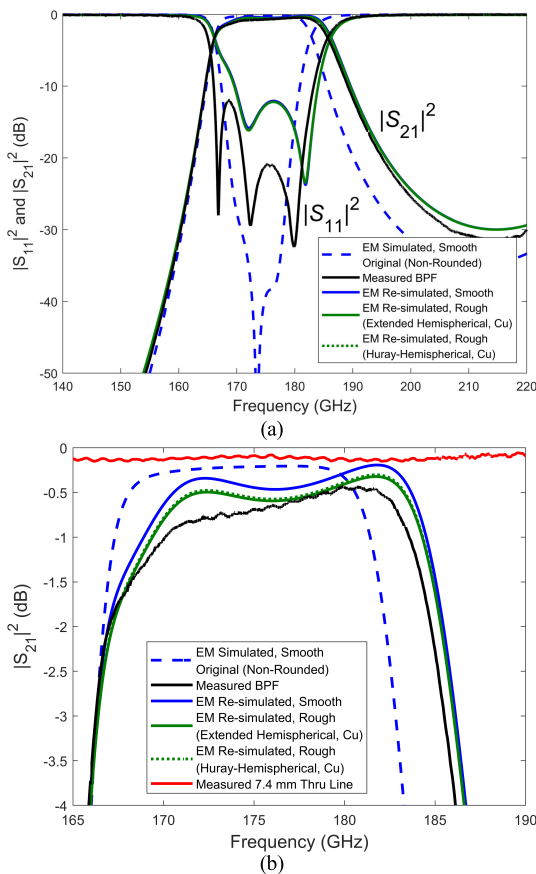

FIGURE 24. EM simulated, measured and EM re-simulated two-port S-parameter responses for the 7.4 mm long 175 GHz BPF, with ICR compensation applied: (a) G-band responses; and (b) close-up passband transmission responses, with the 7.4 mm reference thru line included.

Figure 24 shows the S-parameter responses for the 175 GHz BPF, showing EM simulated, measured and EM re-simulated results. Surface roughness, with the Extended and Huray-Hemispherical models, is again included in the EM re-simulations; the latter not being visible in Fig. 24(a). The measured and re-simulated responses agree well, suggesting that the measured dimensions are accurate.

It can be seen from Fig. 24 that the measured and re-simulated responses for our G-band 5th order filter do not preserve the typical Butterworth approximation, mainly due to underestimating the level of reduction in the iris width values associated with the predicted compensation. Nevertheless, bandpass filtering is achieved.

The minimum insertion loss for this 7.4 mm long BPF is 0.44 dB, at 180 GHz. At this frequency, the reference 7.4 mm thru line has an insertion loss of 0.13 dB, giving a minimum discrepancy of only 0.31 dB when compared with the BPF. With both the BPF and thru line there is a good impedance match at 180 GHz, with return losses better than 20 dB.

There is a slight center frequency up-shift of only 0.5% (0.9 GHz) and a 12.7% (2.2 GHz) increase in 3 dB bandwidth, increasing Q_L from the target value of 10 to the measured value of 11.5.

The minimal passband frequency shifting can be explained by the good fit of the measured cavity lengths and ICR to its predicted compensation values. Here, the measured average ICR radius is 95 μm, compared to the predicted compensation value of $R = 100$ μm. Choosing an accurate R value can be difficult, due to the several factors that influence ICR (discussed previously). Nevertheless, compensation with an R value that approximates the real values is sufficient, as demonstrated by both the 155 GHz and 175 GHz BPFs.

As shown in Table 3, both BPFs compare well with W-band polymer-based 3-D printed symmetrical diaphragm inductive iris BPFs, in terms of passband insertion loss and center frequency shift, despite the higher operational frequencies.

At G-band, our filters demonstrate a comparable frequency shift, and a 2.5 dB insertion loss improvement, when compared to the higher-accuracy metal-based MLS 180 GHz BPF [49]. In contrast to our previous 183 GHz 5th order chained-function filter [9], having a measured minimum insertion loss of 0.55 dB, our new 175 GHz 5th order Butterworth filter exhibits a slightly lower loss of 0.44 dB. Moreover, Q_L significantly decreased from the target value of 10.8 to the measured value of 5.8 [9], while our new 175 GHz filter increased from the target value of 10.0 to the measured value of 11.5; the levels of frequency shift were −0.9% with the previous filter and +0.5% [9] with the new 175 GHz filter.

VII. DISCUSSION AND CONCLUSION

This paper represents the current state-of-the-art in polymer-based 3-D printing of metal-pipe rectangular waveguide components at G-band. The paper starts with a unique and exhaustive up-to-date literature review for 3-D printed MPRWG thru lines, twists and BPFs. This timely review

reveals three main challenges for G-band split-block designs: (i) EM radiation leakage loss; (ii) assembly part alignment; and (iii) manufacturing accuracy limitations. To this end, the authors investigated the design and application of a 'trough-and-lid' assembly solution, using an H-plane a-edge split and lips that extend beyond the sidewalls to connect with the upper wall. This was used to realize thru lines, a 90° twist and symmetrical diaphragm inductive iris-coupled BPFs; the latter two are the first such components to operate above 110 GHz. This split-block solution has also been previously reported by the authors, but without any introduction or discussion. Fabrication was undertaken using an ultra-low-cost desktop MSLA 3-D printer. Our outsourcing plating costs are high, when compared to the 3-D printing, but the overall cost is still low. In-house plating would dramatically reduce this cost.

3-D printed thru line measurements demonstrate an average α'_D across G-band of 12.7 dB/m (0.032 dB/λ_g) for the 7.4 mm exemplar and 13.7 dB/m (0.035 dB/λ_g) for the 10.4 mm exemplar, which compares well with all previously reported D- and G-band 3-D printed thru lines. Commensurate performance to the COTS counterparts is achieved above *ca.* 200 GHz. However, below *ca.* 200 GHz, rectangular-to-trapezoidal cross-sectional distortion (due to lip bending) causes additional attenuation. This was confirmed with EM re-simulations, by applying the measured effective mean aperture width $a_{mean} < a$; the resulting increase in the TE$_{10}$ mode cut-off frequency, from 116 GHz to 130 GHz, significantly increases the level of attenuation in the lower-half of the band. A more robust lip design should be investigated, having a reduced height and increased width, to mitigate lip bending.

Surface roughness modeling was also applied, using the Extended/Huray-Hemispherical models with $K(180\,\text{GHz}) = 1.32$ and 1.28, respectively, adding approximately 2 to 3 dB/m of additional attenuation across G-band. This is the first example of their use with 3-D printed MPRWGs.

The 3-D printed and COTS #1 90° twists exhibit commensurate quantitative worst-case return losses of 13.2 dB and 12.9 dB, respectively. Furthermore, from two-port measurements, both exhibit commensurate qualitative average insertion losses, being approximately 0.62 dB. The retail cost of the measured COTS counterpart is a factor of ×8.5 greater than the manufacturing cost of our ruggedized 3-D printed/plated 90° twist.

Detailed TDR analyses, for the thru lines and the twists, confirm that the flange-to-flange interfaces are the main source of reflections, with a qualitative comparison made between port wave impedance matching. Moreover, when tightly fixed to the measurement setup, the 3-D printed components are mechanically compressed in the longitudinal direction – approximately 0.5 mm (6.8%), 0.9 mm (9.1%) and 1.6 mm (5.0%) for the 7.4 mm thru line, 10.4 mm thru line and the twist, respectively. With the twists, TDR suggests that there is a significant return loss contribution from internal defects in COTS #1, which cannot be verified without destructive visual inspection.

A unique, systematic ICR compensation technique has been applied to two 3-D printed BPFs. As a result, the 155 GHz and 175 GHz exemplars exhibit a low minimum passband insertion loss of 0.47 dB and 0.44 dB, with center frequency up-shifting of only 2.3% and 0.5%, respectively. This compensation technique was previously applied to transverse-offset inductive iris BPFs, but without any introduction or discussion. Further improvement can be expected with: (i) close visual inspection and early part selection/rejection during manufacture; (ii) improved manufacturing process characterization and control; (iii) design iteration; and (iv) the additional application of pixel quantization pre-distortion for MSLA printers (which was beyond the scope of this paper).

The continual advancements in desktop UV photocurable resin printing is leading to significant improvements in dimensional accuracy and surface finish quality. As a result, in the near future, this technology is expected to extend the trough-and-lid assembly solution to MPRWG components to higher frequency bands, a wider range of geometrical complexity (e.g., 90° bends and orthogonal mode transducers), packaging components within the waveguide and integration into subsystems. The trough-and-lid assembly is now a viable solution for new upper-mm-wave MPRWG components. In the not too distant future, with both performance and cost being the main drivers, this paradigm shift in the manufacture of millimeter-wave components and subsystems will inevitably compete with traditional machined technologies; for example, in ubiquitous 5G+ mobile communications and security imaging systems.

REFERENCES

[1] S.-H. Shin, R. Payapulli, L. Zhu, M. Stanley, X. Shang, N. M. Ridler, and S. Lucyszyn, "3-D printed plug and play prototyping for low-cost sub-THz subsystems," *IEEE Access*, vol. 10, pp. 41708–41719, 2022.

[2] S.-H. Shin, X. Shang, N. M. Ridler, and S. Lucyszyn, "Polymer-based 3-D printed 140–220 GHz low-cost quasi-optical components and integrated subsystem assembly," *IEEE Access*, vol. 9, pp. 28020–28038, 2021.

[3] S. Lucyszyn, X. Shang, W. J. Otter, C. W. Myant, R. Cheng, and N. M. Ridler, "Polymer-based 3D printed millimeter-wave components for spacecraft payloads," in *IEEE MTT-S Int. Microw. Symp. Dig.*, Jul. 2018, pp. 1–3.

[4] M. D'Auria, W. J. Otter, J. Hazell, B. T. W. Gillatt, C. Long-Collins, N. M. Ridler, and S. Lucyszyn, "3-D printed metal-pipe mrectangular waveguides," *IEEE Trans. Compon., Packag., Manuf. Technol.*, vol. 5, no. 9, pp. 1075–1092, May 2006.

[5] S.-H. Shin, D. Alyasiri, M. D'Auria, W. J. Otter, C. W. Myant, D. Stokes, Z. Tian, N. M. Ridler, and S. Lucyszyn, "Polymer-based 3-D printed Ku-band steerable phased-array antenna subsystem," *IEEE Access*, vol. 7, pp. 106662–106673, 2019.

[6] E. Marquez-Segura, S.-H. Shin, A. Dawood, N. M. Ridler, and S. Lucyszyn, "Microwave characterization of conductive PLA and its application to a 12 to 18 GHz 3-D printed rotary vane attenuator," *IEEE Access*, vol. 9, pp. 84327–84343, 2021.

[7] W. J. Otter and S. Lucyszyn, "Hybrid 3-D-printing technology for tunable THz applications," *Proc. IEEE*, vol. 105, no. 4, pp. 756–767, Apr. 2017.

[8] W. J. Otter and S. Lucyszyn, "3D printed 1.1 THz waveguides," *Electron. Lett.*, vol. 53, no. 7, pp. 471–473, 2017.

[9] L. Zhu, R. Payapulli, S.-H. Shin, M. Stanley, N. M. Ridler, and S. Lucyszyn, "3-D printing quantization predistortion applied to sub-THz chained-function filters," *IEEE Access*, vol. 10, pp. 38944–38963, 2022.

[10] L. Zhu, S.-H. Shin, R. Payapulli, T. Machii, M. Motoyoshi, N. Suematsu, N. M. Ridler, and S. Lucyszyn, "3-D printed rectangular waveguide 123–129 GHz packaging for commercial CMOS RFICs," *IEEE Microw. Wireless Technol. Lett.*, vol. 33, no. 2, pp. 157–160, Feb. 2023.

[11] Flann Microwave. (2022). *Flann Microwave*. Accessed: Jan. 7, 2023. [Online]. Available: https://flann.com/wp-content/uploads/2022/03/Sub-Millimetre-Seamless-Waveguide-Datasheet-Revision-3.pdf

[12] B. Zhang and H. Zirath, "Metallic 3-D printed rectangular waveguides for millimeter-wave applications," *IEEE Trans. Compon., Packag., Manuf. Technol.*, vol. 6, no. 5, pp. 796–804, May 2016.

[13] *N5250C PNA Series Microwave Network Analyzer System*, 1st ed., Keysight Technologies, Santa Rosa, CA, USA, 2017.

[14] S. Verploegh, M. Coffey, E. Grossman, and Z. Popovic, "Properties of 50–110-GHz waveguide components fabricated by metal additive manufacturing," *IEEE Trans. Microw. Theory Techn.*, vol. 65, no. 12, pp. 5144–5153, Dec. 2017.

[15] J. Shen, M. W. Aiken, M. Abbasi, D. P. Parekh, X. Zhao, M. D. Dickey, and D. S. Ricketts, "Rapid prototyping of low loss 3D printed waveguides for millimeter-wave applications," in *IEEE MTT-S Int. Microw. Symp. Dig.*, Jun. 2017, pp. 41–44.

[16] J. Shen, M. Aiken, C. Ladd, M. D. Dickey, and D. S. Ricketts, "A simple electroless plating solution for 3D printed microwave components," in *Proc. Asia–Pacific Microw. Conf. (APMC)*, Dec. 2016, pp. 1–4.

[17] Virginia Diodes. (2022). *Straight Waveguides, Tapers, Horn Antennae*. Accessed: Jan. 7, 2023. [Online]. Available: https://www.vadiodes.com/en/products/straight-waveguides-tapers-horn-antenna-directional-couplers

[18] A. von Bieren, E. de Rijk, J.-P. Ansermet, and A. Macor, "Monolithic metal-coated plastic components for mm-wave applications," in *Proc. 39th Int. Conf. Infr., Millim., THz waves (IRMMW-THz)*, Sep. 2014, pp. 1–2.

[19] K. Soeda, K. Naganuma, K. Konishi, H. Tamaru, N. Mio, H. Ito, and J. Yumoto, "3D-printed waveguide for 220 GHz–325 GHz band," in *Proc. 47th Int. Conf. Infr., Millim. THz Waves (IRMMW-THz)*, Aug. 2022, pp. 1–2.

[20] H. Yasukochi, "Three-dimensional modeling apparatus, object, and method of manufacturing an object," U.S. Patent 20 120 045 617 A1, Feb. 23, 2012.

[21] J. Shen and D. S. Ricketts, "Additive manufacturing of complex millimeter-wave waveguides structures using digital light processing," *IEEE Trans. Microw. Theory Techn.*, vol. 67, no. 3, pp. 883–895, Mar. 2019.

[22] A. A. Kirilenko, D. Y. Kulik, and L. A. Rud, "Compact 90° twist formed by a double-corner-cut square waveguide section," *IEEE Trans. Microw. Theory Techn.*, vol. 56, no. 7, pp. 1633–1637, Jul. 2008.

[23] M. A. Al-Tarifi and D. S. Filipovic, "Design and fabrication of a full W-band multi-step waveguide 90° twist," *IEEE Microw. Wireless Compon. Lett.*, vol. 26, no. 11, pp. 903–905, Nov. 2016.

[24] G. Chattopadhyay, J. S. Ward, N. Llombert, and K. B. Cooper, "Submillimeter-wave 90° polarization twists R integrated waveguide circuits," *IEEE Microw. Wireless Compon. Lett.*, vol. 20, no. 11, pp. 592–594, Nov. 2010.

[25] J.-Q. Ding, Y. Zhao, and S.-C. Shi, "A full WR-3 band and low-loss 90° waveguide twist based on CNC," *IEEE Trans. THz Sci. Technol.*, vol. 10, no. 1, pp. 93–96, Jan. 2020.

[26] C. Bartlett, D. Miek, F. Kamrath, D. Bruhn, and M. Hoft, "X-band 3D-printed metal-insert twist-component for bandpass filter applications," in *IEEE MTT-S Int. Microw. Symp. Dig.*, Nov. 2021, pp. 329–331.

[27] F. L. Borgne, G. Cochet, J. Haumant, D. Diedhiou, K. Donnart, and A. Manchec, "An integrated monobloc 3D printed front-end in Ku-band," in *Proc. 49th Eur. Microw. Conf. (EuMC)*, Paris, France, Oct. 2019, pp. 786–789.

[28] Q. Liu, Y. Zhang, F. Zhang, and J. Xu, "A 3D printed waveguide hybrid bandpass filter integrated with twisting and bending functionalities," in *Proc. IEEE Int. Symp. Antennas Propag. USNC-URSI Radio Sci. Meeting (AP-S/URSI)*, Jul. 2022, pp. 2000–2001.

[29] O. A. Peverini, M. Lumia, G. Addamo, F. Paonessa, G. Virone, R. Tascone, F. Calignano, G. Cattano, and D. Manfredi, "Integration of an H-plane bend, a twist, and a filter in Ku/K-band through additive manufacturing," *IEEE Trans. Microw. Theory Techn.*, vol. 66, no. 5, pp. 2210–2219, May 2018.

[30] G. Addamo, O. A. Peverini, D. Manfredi, F. Calignano, F. Paonessa, M. Lumia, and G. Virone, "Electromagnetic and mechanical analyses of a 3D-printed Ka-band integrated twist and orthomode transducer," in *IEEE MTT-S Int. Microw. Symp. Dig.*, Jul. 2019, pp. 31–33.

[31] M. García-Vigueras, E. Menargues, T. Debogovic, E. de Rijk, and J. R. Mosig, "Cost-effective dual-polarised leaky-wave antennas enabled by three-dimensional printing," *IET Microw., Antennas Propag.*, vol. 11, no. 14, pp. 1985–1991, 2017.

[32] A. I. Dimitriadis, T. Debogović, M. Favre, M. Billod, L. Barloggio, J.-P. Ansermet, and E. de Rijk, "Polymer-based additive manufacturing of high-performance waveguide and antenna components," *Proc. IEEE*, vol. 105, no. 4, pp. 668–676, Apr. 2017.

[33] Y. Zhang, F. Zhang, Y. Gao, J. Xu, C. Guo, and X. Shang, "3D printed waveguide step-twist with bandpass filtering functionality," *Electron. Lett.*, vol. 56, no. 11, pp. 527–528, May 2020.

[34] Y. Zhang, J. Xu, F. Zhang, X. He, X. Li, Y. Sun, and S. Xu, "A 3-D printed Ka-band twisted waveguide filter with filtering and polarization rotation," in *Proc. IEEE Int. Symp. Antennas Propag. USNC-URSI Radio Sci. Meeting*, Jul. 2019, pp. 1701–1702.

[35] S. Chen, J. Li, Z. Xu, and T. Yuan, "A Ka-band wideband monolithically metallic 3-D printed turnstile junction orthomode transducer with shaped internal profile," in *IEEE MTT-S Int. Microw. Symp. Dig.*, Jun. 2022, pp. 676–679.

[36] J. Shen and D. S. Ricketts, "Compact W-band 'swan neck' turnstile junction orthomode transducer implemented by 3-D printing," *IEEE Trans. Microw. Theory Techn.*, vol. 68, no. 8, pp. 3408–3417, May 2020.

[37] *Product Catalog: Microwave & Millimeter Wave Components & Sub-Assemblies*, MIWV.com, Millimeter Wave Products Inc, St Petersburg, FL, USA, 2023, p. 78.

[38] Flann Microwave Ltd. *Waveguide Twists: Series 450*. Flann.com. Accessed: Jan. 7, 2023. [Online]. Available: http://flann.com/wp-content/uploads/2015/04/Series-450.pdf

[39] Pasternack Enterprises Inc. (2022). *WR-5 90 Degree Right-hand Waveguide Twist*. Accessed: Jan. 7, 2023. [Online]. Available: https://www.pasternack.com/wr-5-90-waveguide-twist-ug387mod-140-220-ghz-pew5tw0002-p.aspx

[40] X. Shang, M. Lancaster, and Y. Dong, "W-band waveguide filter based on large TM_{120} resonators to ease CNC milling," *Electron. Lett.*, vol. 53, no. 7, pp. 488–490, Mar. 2017.

[41] X. Shang, P. Penchev, C. Guo, M. J. Lancaster, S. Dimov, Y. Dong, M. Favre, M. Billod, and E. de Rijk, "W-band waveguide filters fabricated by laser micromachining and 3-D printing," *IEEE Trans. Microw. Theory Techn.*, vol. 64, no. 8, pp. 2572–2580, Aug. 2016.

[42] H. Yang, Y. Dhayalan, X. Shang, M. J. Lancaster, B. Liu, H. Wang, M. Henry, and P. G. Huggard, "WR-3 waveguide bandpass filters fabricated using high precision CNC machining and SU-8 photoresist technology," *IEEE Trans. THz Sci. Technol.*, vol. 8, no. 1, pp. 100–107, Jan. 2018.

[43] J. Hu, S. Liu, S. Zhang, and R. Xu, "Micromachined terahertz waveguide band-pass filters," in *IEEE MTT-S Int. Microw. Symp. Dig.*, Jun. 2017, pp. 650–653.

[44] T. Skaik, Y. Wang, M. Salek, P. Hunyor, H. Wang, P. G. Huggard, T. Starke, M. Attallah, and R. Martinez, "A 3-D printed 300 GHz waveguide cavity filter by micro laser sintering," *IEEE Trans. THz Sci. Technol.*, vol. 12, no. 3, pp. 274–281, May 2022.

[45] J. A. Lorente, M. M. Mendoza, A. Z. Petersson, L. Pambaguian, A. A. Melcon, and C. Ernst, "Single part microwave filters made from selective laser melting," in *Proc. Eur. Microw. Conf. (EuMC)*, Sep. 2009, pp. 1421–1424.

[46] F. Zhang, S. Gao, J. Li, Y. Yu, C. Guo, S. Li, M. Attallah, X. Shang, Y. Wang, M. J. Lancaster, and J. Xu, "3-D printed slotted spherical resonator bandpass filters with spurious suppression," *IEEE Access*, vol. 7, pp. 128026–128034, 2019.

[47] P. Booth and E. V. Lluch, "Enhancing the performance of waveguide filters using additive manufacturing," *Proc. IEEE*, vol. 105, no. 4, pp. 613–619, Apr. 2017.

[48] M. Salek, X. Shang, R. C. Roberts, M. J. Lancaster, F. Boettcher, D. Weber, and T. Starke, "W-band waveguide bandpass filters fabricated by micro laser sintering," *IEEE Trans. Circuits Syst. II, Exp. Briefs*, vol. 66, no. 1, pp. 61–65, Jan. 2019.

[49] T. Skaik, M. Salek, Y. Wang, M. Lancaster, T. Starke, and F. Boettcher, "180 GHz waveguide bandpass filter fabricated by 3D printing technology," in *Proc. 13th U.K.-Eur.-China Workshop Millimetre-Waves THz Technol. (UCMMT)*, Aug. 2020, pp. 1–3.

[50] C. Guo, J. Li, J. Xu, and H. Li, "An X-band lightweight 3-D printed slotted circular waveguide dual-mode bandpass filter," in *Proc. IEEE Int. Symp. Antennas Propag. USNC/URSI Nat. Radio Sci. Meeting*, Jul. 2017, pp. 2645–2646.

[51] B. Al-Juboori, "Lightweight and low-loss 3-D printed millimeter-wave bandpass filter based on gap-waveguide," *IEEE Access*, vol. 7, pp. 2624–2632, 2018.

[52] B. Zhang and H. Zirath, "3D printed iris bandpass filters for millimetre-wave applications," *Electron. Lett.*, vol. 51, no. 22, pp. 1791–1793, Oct. 2015.

[53] K. Fujiwara, R. Kobayashi, S. Kuwahara, S. Takemura, K. Takizawa, and Y. Watanabe, "3-D printed iris waveguide filter in W-band," in *Proc. 23rd Int. Microw. Radar Conf. (MIKON)*, Warsaw, Poland, Oct. 2020, pp. 346–349.

[54] *IEEE Standard for Rectangular Metallic Waveguides and Their Interfaces for Frequencies of 110 GHz and Above—Part 1: Frequency Bands and Waveguide Dimensions*, Standard 1785.1-2012, 2012.

[55] *IEEE Standard for Rectangular Metallic Waveguides and Their Interfaces for Frequencies of 110 GHz and Above—Part 2: Waveguide Interfaces*, Standard IEEE 1785.2–2016, 2016.

[56] K. Fujiwara, R. Kobayashi, S. Kuwahara, S. Takemura, K. Takizawa, and Y. Watanabe, "3-D printed iris waveguide filter in W-band," in *Proc. 23rd Int. Microw. Radar Conf. (MIKON)*, Oct. 2020, pp. 346–349.

[57] A. Pons, J. M. García, F. D. Quesada, A. Alvarez-Melcon, A. Romera, J. Hinojosa, M. Guglielmi, V. E. Boria, and L. Arche-Andradas, "Evanescent mode filters composed of dielectric parts built using 3D-printing methods," in *IEEE MTT-S Int. Microw. Symp. Dig.*, Perugia, Italy, Nov. 2021, pp. 14–16.

[58] M. V. Mrvić, M. M. Potrebić, and D. V. Tošić, "Compact H-plane dual-band bandstop waveguide filter," *J. Comput. Electron.*, vol. 16, no. 3, pp. 939–951, Jun. 2017.

[59] X. Shang, P. Klasmann, and M. J. Lancaster, "A compact Ka-band waveguide orthomode transducer fabricated by 3-D printing," in *Proc. 46th Eur. Microw. Conf. (EuMC)*, Oct. 2016, pp. 365–368.

[60] S. M. Lewis, E. A. Nanni, and R. J. Temkin, "Direct machining of low-loss THz waveguide components with an RF choke," *IEEE Microw. Wireless Compon. Lett.*, vol. 24, no. 12, pp. 842–844, Dec. 2014.

[61] N. Jastram, M. A. Altarifi, L. Boskovic, and D. S. Filipovic, "On the split-block realization of millimeter-wave ridge waveguide components," *IEEE Microw. Wireless Compon. Lett.*, vol. 28, no. 4, pp. 296–298, Apr. 2018.

[62] J. Hesler, "A photonic crystal joint (PCJ) for metal waveguides," in *IEEE MTT-S Int. Microw. Symp. Dig.*, May 2001, pp. 783–786.

[63] Microwaves101. (2022). *Waveguide Construction*. Accessed: Jan. 7, 2023. [Online]. Available: https://www.microwaves101.com/encyclopedias/waveguide-construction

[64] Millimeter Wave Products Inc. (2022). *75 GHz to 110 GHz, Harmonic Mixer*. Accessed: Jan. 7, 2023. [Online]. Available: https://www.miwv.com/920w-387-harmonic-mixer-f-frequency-range-75-ghz-to-110-ghz-lo-frequency-range-2-ghz-to-20-ghz-lo-drive-level-10-dbm/

[65] J. Hong and M. Lancaster, *Microstrip Filters for RF/Microwave Applications*, 1st ed. Hoboken, NJ, USA: Wiley, 2001.

[66] R. J. Cameron, C. M. Kudsia, and R. R. Mansour, *Microwave Filters for Communication Systems: Fundamentals, Design and Applications*, 2nd ed. Hoboken, NJ, USA: Wiley, 2018.

[67] Elegoo Inc. (2021). *Elegoo Mars 2 Pro Mono LCD MSLA Resin 3D Printer*. Accessed: Jan. 7, 2023. [Online]. Available: https://www.elegoo.com/products/elegoo-mars-2-pro-mono-lcd-3d-printer

[68] Chitubox. (2021). *CHITUBOX, All-in-One SLA/DLP/LCD Slicer, 3D Printing Preprocessing Software*. Accessed: Jan. 7, 2023. [Online]. Available: https://www.chitubox.com/en/page/chitubox-free

[69] Pasternack Enterprises Inc. (2022). *WR-5 Straight Waveguide Section 1 Inch Length, UG-387/U-Mod Round Cover Flange From 140 GHz to 220 GHz*. Accessed: Jan. 7, 2023. [Online]. Available: https://www.pasternack.com/wr-5-straight-waveguide-section-ug387-mod-round-pew05s000-1-p.aspx

[70] Fairview Microwave Inc. (2022). *WR-5 Waveguide Section 1 Inch Straight Length With UG-387/U-Mod Round Cover Flange From 140 GHz to 220 GHz*. Accessed: Jan. 7, 2023. [Online]. Available: https://www.fairviewmicrowave.com/wr-5-waveguide-section-straight-ug387-mod-round-fmw05s000-1-p.aspx

[71] Hasco Components Inc. (2022). *Waveguide, WR-5, 1-Inch Straight Section, 140 GHz to 220 GHz, G-Band*. Accessed: Jan. 7, 2023. [Online]. Available: https://www.hasco-inc.com/waveguide-components/wr-5-millimeter-waveguide-1-inch-straight-section-140-ghz-to-220-ghz-g-band/

[72] Fairview Microwave Inc. (2022). *WR-5 90 Degree Waveguide Right-hand Twist Using a UG-387/U-Mod Flange and a 140 GHz to 220 GHz Frequency Range*. Accessed: Jan. 7, 2023. [Online]. Available: https://www.fairviewmicrowave.com/wr-5-90-waveguide-twist-ug387mod-140-220-ghz-fmw5tw0002-p.aspx

[73] Hasco Components Inc. (2022). *Waveguide Section, 90 Degree Twist, 1-Inch Section, 140 GHz to 220 GHz, G-Band*. Accessed: Jan. 7, 2023. [Online]. Available: https://www.hasco-inc.com/waveguide-components/wr-5-millimeter-waveguide-90-degree-twist-1-inch-section-140-ghz-to-220-ghz-g-band/

[74] P. G. Huray, O. Oluwafemi, J. Loyer, E. Bogatin, and X. Ye, "Impact of copper surface texture on loss: A model that works," *DesignCon*, vol. 1, pp. 462–483, Jun. 2010.

[75] E. Hammerstad and O. Jensen, "Accurate models for microstrip computer-aided design," in *IEEE MTT-S Int. Microw. Symp. Dig.*, May 1980, pp. 407–409.

[76] S. Groiss, I. Bardi, O. Biro, K. Preis, and K. R. Richter, "Parameters of lossy cavity resonators calculated by the finite element method," *IEEE Trans. Magn.*, vol. 32, no. 3, pp. 894–897, May 1996.

[77] S. Hall, S. G. Pytel, P. G. Huray, D. Hua, A. Moonshiram, G. A. Brist, and E. Sijercic, "Multigigahertz causal transmission line modeling methodology using a 3-D hemispherical surface roughness approach," *IEEE Trans. Microw. Theory Techn.*, vol. 55, no. 12, pp. 2614–2624, Dec. 2007.

[78] Q. Chen, H. W. Choi, and N. Wong, "Robust simulation methodology for surface-roughness loss in interconnect and package modelings," *IEEE Trans. Comput.-Aided Design Integr. Circuits Syst.*, vol. 28, no. 11, pp. 1654–1665, Nov. 2009.

[79] S. Bakirtzis, X. Zhang, and C. D. Sarris, "Stochastic modeling of wave propagation in waveguides with rough surface walls," *IEEE Trans. Microw. Theory Techn.*, vol. 69, no. 1, pp. 500–508, Jan. 2021.

[80] S. H. Hall and H. L. Heck, *Advanced Signal Integrity for High-Speed Digital Designs*, 1st ed. Hoboken, NJ, USA: Wiley, 2009.

[81] J. D. Jackson, *Classical Electrodynamics*, 3rd ed. Hoboken, NJ, USA: Wiley, 1999.

[82] D. M. Pozar, *Microwave Engineering*, 4th ed. Hoboken, NJ, USA: Wiley, 2012.

[83] N. Shoaib, N. M. Ridler, and M. J. Salter, "Commissioning of the NPL WR-05 waveguide network analyser system for S-parameter measurements from 140 GHz to 220 GHz," NPL, Nat. Phys. Lab., Teddington, U.K., Tech. Rep. TQE 12, Mar. 2015.

[84] Virginia Diodes Inc. (2022). *VNA Extender VDI Model: WR5.1-VNAX*. Accessed: Jan. 7, 2023. [Online]. Available: https://www.vadiodes.com/index.php/en/products/vector-network-analyzer?id=853

[85] R. Wenger, *1-Inch Self-Symmetric Straight*. Charlottesville, VA, USA: Virginia Diodes Inc., May 2014.

[86] F. L. Warner, "Attenuation measurement," in *Microwave Measurements*, 2nd ed., A. E. Bailey, Ed. London, U.K.: IEE, 1989, pp. 132–134.

[87] S. Lucyszyn, "RFIC and MMIC measurement techniques," in *Microwave Measurements*, 3rd ed., R. J. Collier and A. D. Skinner, Eds. London, U.K.: IET, Oct. 2007, pp. 217–262.

[88] A. H. Nuttall, "Some windows with very good sidelobe behavior," *IEEE Trans. Acoust., Speech, Signal Process.*, vol. ASSP-29, no. 1, pp. 84–91, Feb. 1981.

[89] J. Sun and S. Lucyszyn, "Extracting complex dielectric properties from reflection-transmission mode spectroscopy," *IEEE Access*, vol. 6, pp. 8302–8321, 2018.

[90] J. Sun, A. Dawood, W. J. Otter, N. M. Ridler, and S. Lucyszyn, "Microwave characterization of low-loss FDM 3-D printed ABS with dielectric-filled metal-pipe rectangular waveguide spectroscopy," *IEEE Access*, vol. 7, pp. 95455–95486, 2019.

MANOJ STANLEY (Member, IEEE) received the Ph.D. degree in electrical engineering from the University of Liverpool, in 2019. After the completion of his Ph.D., he joined the National Physical Laboratory, U.K., as a Higher Research Scientist with the Electromagnetic Technologies Group. He has supported the development of next-generation computing and communications technologies and high-frequency electronics applications. This includes the design and characterization of devices at RF and terahertz frequencies, RF metrology for quantum computing applications, and material and channel characterization for 5G and beyond communications. Currently, he is developing high-frequency metrology capabilities to characterize superconducting quantum integrated circuits at milli-Kelvin temperatures. He was the Operations Officer of European Microwave Week, in 2021.

ROSHAN PAYAPULLI received the M.Eng. degree in electrical and electronic engineering from Imperial College London, London, U.K., in 2018, where he is currently pursuing the Ph.D. degree with the Department of Electrical and Electronic Engineering.

His research interests include designing and manufacturing lightweight and low-cost waveguide components and systems for microwave and millimeter-wave applications using additive manufacturing techniques.

NICK M. RIDLER (Fellow, IEEE) received the B.Sc. degree from King's College London, University of London, London, U.K., in 1981. He is the Head of Science with the Electromagnetic and Electrochemical Technologies Department, National Physical Laboratory (NPL), U.K. He is also an NPL Fellow; an Honorary Professor with the University of Glasgow, U.K., and University of Liverpool, U.K.; and a Visiting Professor with the University of Kent, University of Leeds, and University of Surrey, U.K. He is also a Non-Executive Director of LA Techniques Ltd., and a fellow of the Institution of Engineering and Technology (IET) and the Institute of Physics (IOP). He has more than 35 years' experience in industrial, government, and academic research establishments. His research interest includes precision high-frequency electromagnetic measurement (from 1 kHz to 1 THz).

LIYAN ZHU received the B.Eng. degree in electronic science and technology from the Huazhong University of Science and Technology (HUST), Wuhan, China, in 2018, and the M.Sc. degree in telecommunications from University College London (UCL), London, U.K., in 2019. He is currently pursuing the Ph.D. degree with the Department of Electrical and Electronic Engineering, Imperial College London, London. His research interests include the design, fabrication, and sensitivity analysis of microwave components using additive manufacturing techniques.

STEPAN LUCYSZYN (Fellow, IEEE) received the Ph.D. degree in electronic engineering from King's College London, University of London, London, U.K., in 1992, and the D.Sc. degree (Hons.) in millimeter-wave and terahertz electronics from Imperial College London, London, in 2010.

He is currently a Professor of millimeter-wave systems with Imperial College London. He has coauthored well over 200 articles and 12 book chapters in applied physics and electronic engineering. He was a fellow of the Institution of Electrical Engineers, U.K., and the Institute of Physics, U.K., in 2005. In 2008, he became a fellow of the Electromagnetics Academy, USA. He has co-founded Imperial College London spin-out company Drayson Wireless Ltd., in 2014. In 2022, for their work on 3-D printing, he and his team at Imperial College London won Junkosha's Inaugural Technology Innovator of the Year Award for the microwave and millimeter-wave category. He was an IEEE Distinguished Microwave Lecturer, from 2010 to 2013.

SANG-HEE SHIN (Member, IEEE) was born in Seoul, South Korea, in 1992. He received the M.Eng. degree in aeronautical engineering and the Ph.D. degree in electrical and electronic engineering from Imperial College London, London, U.K., in 2018 and 2022, respectively. He recently joined the National Physical Laboratory, U.K., as a Higher Research Scientist with the Department of Electromagnetic and Electrochemical Technologies. His research interests include designing and manufacturing RF and quasi-optical devices for microwave and millimeter-wave applications using additive manufacturing techniques.

• • •